

GECO: Galaxy Evolution COde - A new semi-analytical model of galaxy formation

E. Ricciardelli^{1,2,3} and A. Franceschini¹

¹Dipartimento di Astronomia, Università di Padova, Vicolo Osservatorio 2, 35122 Padova, Italy

²Instituto de Astrofísica de Canarias, Vía Lactea s/n, E-38200 La Laguna, Tenerife, Spain

³Departamento de Astrofísica, Universidad de La Laguna, E-38205, Tenerife, Spain

Accepted 16/04/2010 Received ...; in original form ...

ABSTRACT

Aims. We present a new semi-analytical model of galaxy formation, GECO (Galaxy Evolution COde), aimed at a better understanding of when and how the two processes of star formation and galaxy assembly have taken place, by comparison with a wide variety of recent data on the evolutionary galaxy mass functions and star-formation histories.

Methods. Our model is structured into a Monte Carlo algorithm based on the Extended Press-Schechter theory, for the representation of the merging hierarchy of dark matter halos, and a set of analytic algorithms for the treatment of the baryonic physics, including classical recipes for the gas cooling, the star formation time-scales, galaxy mergers and SN feedback. Together with the galaxies, the parallel growth of BHs is followed in time and their feedback on the hosting galaxies is modelled. We set the model free parameters by matching with data on local stellar mass functions and the BH-bulge relation at $z = 0$.

Results. Based on such local boundary conditions, we investigate how data on the high-redshift universe constrain our understanding of the physical processes driving the evolution, focusing in particular on the assembly of stellar mass and on the star formation history. Since both processes are currently strongly constrained by cosmological near- and far-IR surveys with the Spitzer Space Telescope, the basic physics of the Λ CDM hierarchical clustering concept of galaxy formation can be effectively tested by us by comparison with the most reliable set of observables using a minimal number of free parameters.

Conclusions. Our investigation shows that when the time-scales of the stellar formation and mass assembly are studied as a function of dark matter halo mass and the single galaxy stellar mass, the 'downsizing' fashion of star formation appears to be a natural outcome of the model, reproduced even in the absence of the AGN feedback. On the contrary, the stellar mass assembly history turns out to follow a more standard hierarchical pattern progressive in cosmic time, with the more massive systems assembled at late times mainly through dissipationless mergers.

Key words. galaxies: evolution – galaxies: formation – galaxies: halos.

1. Introduction

In the past decade, several observational evidences were accumulating in favour of the Λ CDM paradigm for structure formation, now quite a successful rendition of the hierarchical clustering scenario for cosmic structure formation. In its standard form (Blumenthal et al., 1984), it predicts that structures formed from primordial fluctuations of the density field amplified during inflation and then collapsed to form the virialized structures that we see nowadays. The most compelling support in favour of this paradigm comes from the measurements of the temperature anisotropies of the cosmic microwave background (Spergel et al., 2003, 2007). Further evidences are due to the measurements of the power spectrum of galaxy clustering from large surveys of the local universe (Percival et al., 2002; Tegmark et al., 2004), the evidence for an accelerated expansion of the universe as inferred from high-redshift type Ia supernovae observations (Riess et al., 1998; Perlmutter, Turner, & White, 1999) and the baryon fraction observed in rich clusters (White et al., 1993).

Devised to study galaxy evolution within this cosmological framework, the semi-analytical approach favours a relatively

simple handling of the main physical parameters and understanding of their possible role in driving the evolution. This modelling has its root in the work of White & Rees (1978), where it was proposed that galaxy formation is a two-stage process, with dark matter halos forming in a dissipationless gravitational collapse and galaxies forming inside them following the radiative cooling of baryons. Although White & Rees (1978) and, after, White & Frenk (1991), based their work only on the analytic Press-Schechter theory (Press & Schechter, 1974), predicting only average quantities, subsequently a number of works followed their prescriptions using Monte Carlo (MC) merger trees. The MC approach allows to obtain several realizations of the merging history of individual dark matter halos. This approach was pioneered by Lacey & Cole (1993); Kauffmann & White (1993); Cole et al. (1994), and then followed by a number of authors (Somerville & Kolatt, 1999; Sheth & Lemson, 1999; Zentner, 2007). The great advantage of the semi-analytical method (SAM), apart from being computationally very fast and flexible, is the fact that it is possible to compute merging histories with arbitrary mass resolution. The alternative approach that can be followed in order to track the evolution of the dark matter halos, is through the use of large cosmological N-body simulations. Their large computational requirements are compensated by the amount of information that

Send offprint requests to: Elena Ricciardelli,
e-mail: elenaricci@iac.es

can be achieved. For instance, in the Millennium Simulation (Springel, Yoshida, & White, 2001), the evolution of substructures in massive halos can be followed in time, with the results of a more detailed information about the galaxy dynamics and the influence of the cosmic environment on the process (De Lucia et al., 2004). In the literature, various examples of this “hybrid” approach, which make use of N-body simulation for the dark matter evolution and the SAM technique for the baryonic physics, have been published (Hatton et al., 2003; De Lucia et al., 2006; Croton et al., 2006).

In the present work we employ a MC merger tree, mainly because this allowed us to test the parameter space of the semi-analytical model with much more flexibility than using N-body simulations, and allows to compute merging histories down to arbitrary low mass resolution.

While the treatment of the evolution of dark matter structures is relatively simple, as being determined only by gravity, the physics of the baryons inside halos is much more complex to describe. In the most classical models (Kauffmann, White, & Guiderdoni, 1993; Baugh, Cole, & Frenk, 1996; Kauffmann et al., 1999; Somerville & Primack, 1999; Cole et al., 2000; Menci & Cavaliere, 2002), gas cooling, star formation, SN feedback and galaxy mergers are included. In recent years, it has become clear that some other form of highly energetic feedback is needed to prevent star formation in massive galaxies at recent epochs, where the SN feedback is ineffective. The need of such form of feedback is required in order to avoid the overcooling in massive halos, and hence the overabundance of galaxies at the bright-end of the luminosity function. This source of feedback is commonly found in the AGN energy production. This effect, supported by the observational findings of a tight correlation between the BH and the bulge size (Ferrarese & Merritt, 2000; Häring & Rix, 2004), was implemented in different ways by Kauffmann & Haehnelt (2000); Bower et al. (2006); Croton et al. (2006); Menci et al. (2006); Somerville et al. (2008).

Alternative to the AGN feedback, the shutdown of star formation above a critical halo mass has been implemented as a quenching mechanism in massive galaxies (Cattaneo et al., 2006, 2008), motivated by the prediction of stable shock heating for halos more massive than this threshold (Dekel & Birnboim, 2006).

Following the prescriptions of these models, we have built a new semi-analytical models, the Galaxy Evolution COde (GECO), whose aim is to identify a few key physical parameters and modify them by comparing with several basic properties of the galaxy population at $z = 0$, as well as at high redshifts. Our main observational reference in this paper is the redshift-dependent stellar mass function of galaxies, which, from a suitable choice for the stellar Initial Mass Function (IMF), is a robust descriptor of the star formation history and the mass assembly history of galaxies.

The structure of the paper is as follows. In §2 we describe the Monte Carlo merger tree used in the model. In §3 we introduce the ingredients of the baryonic model. In §4 we explain how the free parameters are set and provide a table for them. In §5 the basic results for the local universe are presented, while in §6 we focus on the high redshift predictions. We conclude in §7. Throughout the rest of the paper we assume a “concordance” cosmological model, with $\Omega_m = 0.3$, $\Omega_\Lambda = 0.7$, $h = 0.7$, $\sigma_8 = 0.9$ and $n = 1$ (power index of the primordial power spectrum). However, when needed, we also show the dependence on the cosmological parameters showing the results for

the new WMAP5 dataset, which are: $\Omega_m = 0.258$, $\Omega_\Lambda = 0.742$, $h = 0.719$, $\sigma_8 = 0.796$ and $n = 0.963$ (Dunkley et al., 2009).

2. Merger Tree

2.1. The formalism

In the hierarchical theory of structure formation the density contrast $\delta = (\rho - \rho_b)/\rho_b$, where ρ_b is the mean density of the universe and ρ is the perturbation density, is a Gaussian random field that at early times grows linearly. When the density contrast reaches a critical value δ_c , given by the spherical collapse theory, the perturbation starts to collapse and form virialized halos. In order to associate masses to these collapsed objects, the Press-Schechter approach considers the fluctuations whose density contrast smoothed on a scale R_M , through a spatial window function $W(r, R_M)$, exceeds δ_c .

The Gaussian random variable δ has zero mean and variance $S(M) = \sigma^2(M)$ which is linked to the mass through the Power-spectrum $P(k)$:

$$\sigma^2(M) = \frac{1}{2\pi^2} \int P(k)W^2(kr)k^2 dk, \quad (1)$$

where $W^2(kr)$ is the Fourier transform of the spatial window function. In the excursion-set approach, developed by Bond et al. (1991), the value of δ executes a random walk as the smoothing scale R_M (or M) is changed. We can consider the trajectories in the plane (S, δ_c) and associate the fraction of matter in collapsed objects in the range dM around M at the time t with the fraction of trajectories that make the first upcrossing through the threshold δ_c in the interval $S, S + dS$. This results in the well-known PS mass function:

$$f(S, \delta_c)dS = \frac{1}{\sqrt{2\pi}} \frac{\delta_c}{S^{3/2}} \exp\left(-\frac{\delta_c^2}{2S}\right)dS \quad (2)$$

(Press & Schechter, 1974).

In the *Extended Press-Schechter* model (Bond et al., 1991; Lacey & Cole, 1993) it is also possible to derive the conditional mass function, the fraction of trajectories in halos with mass M_1 at z_1 that are in halos with mass $M_0 > M_1$ at $z_0 < z_1$:

$$f(S_1, \delta_{c1}|S_0, \delta_{c0})dS_1 = \frac{1}{\sqrt{2\pi}} \frac{(\delta_{c1} - \delta_{c0})}{(S_1 - S_0)^{3/2}} \exp\left[-\frac{(\delta_{c1} - \delta_{c0})^2}{2(S_1 - S_0)}\right]dS_1. \quad (3)$$

Converting from mass weighting to number weighting we obtain the average number of progenitors at z_1 in the mass interval dM_1 around M_1 which at redshift z_0 has merged to form an M_0 halo:

$$\frac{dP}{dM_1}(M_1, z_1|M_0, z_0)dM_1 = \frac{M_0}{M_1} f(S_1, \delta_{c1}|S_0, \delta_{c0}) \left| \frac{dS}{dM} \right| dM_1. \quad (4)$$

2.2. The partition algorithm

For generating Monte Carlo realizations of the merging history of dark matter halos we use the partition algorithm described by Sheth & Lemson (1999), hereafter SL99, which is exact for a white-noise power-spectrum, but needs some modifications in order to be applied to a Λ CDM fluctuation spectrum. Since we will describe in detail the algorithm and the test done to probe

its consistency in a separate paper, we give here only a brief description of it.

The algorithm is based on the assumption that for a white-noise spectrum mutually disconnected volumes are mutually independent, as it is analytically demonstrated in the Appendix of SL99. Let us call *parent* the halo of mass M_0 which exists at $z=0$ and *progenitors* the smaller halos that derive from it at higher redshift. Suppose to partition an halo of mass M_0 into progenitors by choosing first one progenitor and then an other one from the remaining mass and so on until the remaining mass falls below a certain minimum mass that is our mass resolution M_{res} . We have a probability of finding the first progenitor of mass M_1 , corresponding to S_1 , given by $f(S_1, \delta_{c1}|S_0, \delta_{c0})$ (equation 3) and we choose a mass drawing a random number from this distribution. We can consider the halo M_0 as a region of size $V_{M_0} = M_0 b_0 / \rho_b$, where $b_0 = 1/(1+\delta_0)$. If the first progenitor has mass M_1 it occupies a volume $V_{M_1} = M_1 b_1 / \rho_b$. The remaining mass $R = M_0 - M_1$ is distributed in the volume $V_R = R b_R / \rho_b$. Hence, for the conservation of volumes, the density in this region is given by

$$\delta_{cR} = \delta_{c1} - \frac{(\delta_{c1} - \delta_{c0})}{1 - (M_1/M_0)} \quad (5)$$

to lowest order in δ (see equation 5 of SL99). Now, the second progenitor must be chosen from the remaining mass R and the probability that it has mass M_2 , corresponding to S_2 , is given by $f(S_2, \delta_{c2}|S(R), \delta_{cR})$. Therefore we choose a random number from this distribution. Then we iterate the process by continuing to find progenitors until the remaining mass is below the mass resolution.

The assumption that disconnected volumes are mutually independent is right only for white noise power spectrum, but we want to build merger trees for a Λ CDM spectrum. SL99 show that by applying the same algorithm for scale-free spectra with $n \neq 0$ leads to inconsistencies in the excursion set mean values. Since we know that all the excursion set quantities are independent of the power spectrum when they are expressed in terms of the variance rather than the mass, we run the algorithm for the white-noise case. Then we consider each chosen M_{wn} not as a progenitor with mass M_{wn} , but as a region populated by some number ν of objects having mass $M_{\Lambda CDM}$. In practise, we normalize the white-noise power spectrum in such a way that the mass variance of the two spectra is the same in M_0 : $S_0 = S_{\Lambda CDM}(M_0)$. Then, we choose S_1 from the distribution of equation 3. We associate to this variance a mass given by the white-noise spectrum $M_{wn} = S_0 M_0 / S_1$ and one given by the Λ CDM spectrum $M_{\Lambda CDM}$. We consider a number ν of halos with this mass, given by $\nu = M_{wn} / M_{\Lambda CDM}$, approximated to the nearest integer. Then, we iterate the procedure on each new progenitor.

As a test of the consistency of our MC merger tree with the PS predictions, in Figure 1 we show the global mass function of dark matter halos. To compute it, we use a grid of 35 parent halo masses, ranging from $10^{10} M_\odot$ to $10^{15} M_\odot$, logarithmically spaced, and simulate 100 realizations for each parent halo. Then we weight each halo with the PS number density at $z=0$. The results do not depend much on the number of parent halo masses used, but they are quite sensitive to the number of realizations for each halo. The 100 realizations used turn out to be a good compromise between the good sampling desired and the computational-time required. We build a grid in time of 52 intervals logarithmically spaced in redshift, ranging from $z=20$ when the time-step is approximately equal to 0.05 Gyr to $z=0$ with a ~ 0.8 Gyr time-step. Because our method for building merger

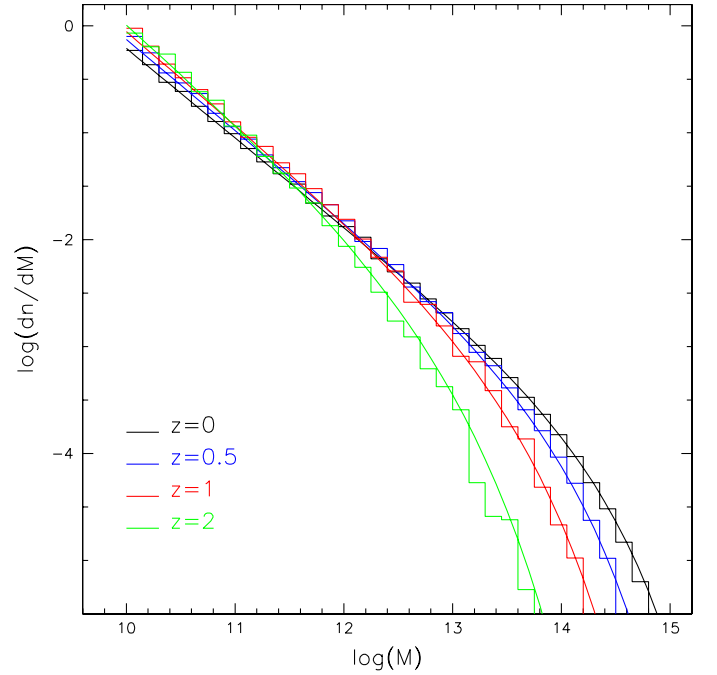


Fig. 1. Global mass function for dark matter halos at different redshifts. Histograms represent the mass function derived from our MC merger tree, while solid lines show the PS predictions.

tree is insensitive to the time-step used, the choice of the time-step grid is quite arbitrary and we are not forced to use too small time intervals. We find very good agreement between the MC method and the analytical predictions. A key point of this algorithm is that it correctly reproduces the mean statistical quantities of EPS and PS predictions for any set of M_1, z_1, M_0, z_0 . This means that there is no need to divide the time interval between z_0 and z_1 in smaller time-steps. This is particularly convenient because it allows us to choose the time grid for the semi-analytical implementation in an arbitrary way.

The algorithm described is based on the Extended Press-Schechter formalism, that means on the spherical barrier model, but it can be extended for a more general moving barrier model, useful for the description of the ellipsoidal collapse model (Bond & Myers, 1996) that bears closer consistency with N-body simulation (Sheth & Tormen, 2002; Giocoli et al., 2007; Zentner, 2007; Zhang, Ma, & Fakhouri, 2008).

3. The baryonic model

While the theory of the hierarchical development of the dark matter structures is relatively simple and now well established, the complex physics of baryons presents still highly uncertain aspects, and requires the treatment of several processes in a simplified form. The latter is obtained with the introduction of a minimum number of free parameters in the model, that can only be set through a comparison of the model predictions with observational data. These parameters flag our lack of knowledge about the details of the physics of galaxy formation. Obviously, although they are set by fitting model results with observations, only limited ranges of values are allowed: values outside these would indicate fundamental problems in the process treatment or lack of important physical ingredients. This Section is dedicated to a description of our new SAM model, GECO.

At variance with the majority of the models of galaxy formation, we tested our results directly on the observables involving stellar mass rather than luminosities, to avoid introducing further uncertainties in the model due to the spectro-photometric synthesis, dust extinction and the Initial Mass Function. The elaboration of the photometric synthesis based on the model galaxy mass function will be deferred to a future work.

3.1. Linking Galaxies to Dark Matter Halos

As described in the previous section, the generation of the merger tree proceeds backwards in time. Starting from the initial redshift (typically $z = 0$), we split each halo into progenitors at higher redshifts. On the contrary, galaxy formation is modelled forward in time, starting from the “leaves” of the tree, i.e. halos at high redshift whose progenitors fall below the mass limit resolution ($M_{res} = 10^{10} M_{\odot}$ in our case) and their hierarchy is no more followed in time. Starting from each of these halos we put baryons inside them, according to the baryonic fraction observed by WMAP5: $f_b = \Omega_b/\Omega_m = 0.17$ (Dunkley et al., 2009).

We use the grid in parent halo masses and time-steps described in Sect. 2.2. To solve the differential equations for baryon evolution that we are going to introduce in the following sections, we divide each step of the merger hierarchy into 100 smaller substeps which allow us to solve the system of equations through the use of finite increments of mass.

In order to derive statistical quantities such as the mass function or the SFR density, we simply make a weighted sum over the model galaxies. Since we are dealing with an EPS merger tree, we use for consistency as a weight scheme the number density of halos given by the PS mass function. In some cases, we have also checked the results using a Sheth & Tormen number density (Sheth & Tormen, 2002), which fits the results of N-body simulations with higher accuracy, but we have found that it makes little difference.

We will describe in the following the baryonic processes at work in driving the evolution of galaxies, starting from the cooling of the gas.

3.2. Dynamical Time-scales and Gas Cooling

The cooling of the gas is a fundamental process for galaxy formation, as it sets the rate at which gas becomes available for star formation. The first to invoke the need of some dissipative process occurring inside dark matter halos were White & Rees (1978), in order to explain the difference between the luminosity function of galaxies, with its characteristic mass and size, and the halo mass function, that on galactic scales is a typical power-law without any preferred scales. White & Rees argued that galaxy formation is a two stage process, with dark matter halos forming through the dissipationless hierarchical clustering, and with gas cooling occurring inside them.

The gas is assumed to be heated by shocks during the violent relaxation following the collapse, up to the virial temperature of the halo, given by:

$$T = \frac{1}{2} \frac{\mu m_H}{k} V_c^2, \quad (6)$$

where μ is the mean molecular mass of the gas, m_H is the mass of a hydrogen atom, k is the Boltzmann’s constant and V_c is the circular velocity of the halo, that can be related to the mass of the halo through the expression: $V_c = \sqrt{GM_{halo}/R_{vir}}$. The virial radius, R_{vir} , is the limiting radius

of a virial halo, within which the mean density is $200\rho_c$, where ρ_c is the universal critical density, and is given by $R_{vir} = 1.63 \times 10^{-2} (M_{halo}/M_{\odot} h^{-1})^{1/3} (\Omega(z)/\Omega_m)^{1/3} (1+z)^{-1} h^{-1} kpc$ (Navarro, Frenk, & White, 1997). From V_c and the virial radius R_{vir} , an halo dynamical time can be defined:

$$t_{halo} = R_{vir}/V_c. \quad (7)$$

The rate at which the gas cools depends upon this temperature, which determines its ionization state, and on the metallicity of the gas, that is the chemical composition. We take the cooling function $\Lambda(T, Z)$ tabulated by Sutherland & Dopita (1993). Note that the cooling function also depends on the metallicity of the hot gas. High metallicity values increase the cooling rate, because of line cooling from heavy elements, mainly for low-mass halos. We assume that the hot gas has a constant metallicity equal to $0.3Z_{\odot}$, close to the value for the hot gas in cluster (Somerville et al., 2008). We have also checked that by adopting a solar metallicity instead of the subsolar one, the results do not change significantly.

The cooling time is defined as the thermal energy density divided by the cooling rate per unit volume:

$$t_{cool} = \frac{3}{2} \frac{\mu m_H k T}{\Lambda(T, Z) \rho_{gas}}, \quad (8)$$

where ρ_{gas} is the gas density profile, which is assumed to be isothermal:

$$\rho_{gas}(r) = \frac{M_{hot}}{4\pi R_{vir} r^2}, \quad (9)$$

where M_{hot} is the total gas mass in the hot component, which is assumed to extend to the virial radius. A cooling radius, r_{cool} , can now be defined as the point where the local cooling time is equal to the age of the universe at that epoch.

We can now compute the rate at which gas accretes to the centre of the halo, becoming available for star formation. Following the treatment of White & Frenk (1991), we distinguish two regime of cooling, depending on the value of r_{cool} . The first case corresponds to $r_{cool} > R_{vir}$, the cooling radius lying outside the virialized region of the halo. The cooling is so rapid that the infalling gas never reaches the hydrostatic equilibrium and the supply of cold gas for star formation is limited by the infall rate rather than the cooling rate. We assume that all the hot gas in the halo will settle to the centre in a time-scale given by the halo dynamical time:

$$\dot{M}_{cool} = \frac{M_{hot} V_c}{R_{vir}}. \quad (10)$$

This regime of cooling was called by White & Frenk (1991) the *rapid cooling regime*, also known as *cold mode*.

The second way of infalling is the static hot halo regime, or *hot mode*, that occurs when the cooling radius lies inside the virial radius. In this case, the gas inside r_{cool} will be pressure-supported and will contract quasi-statically toward the centre. Cooling will cause a flow of gas toward the centre in a way exactly analogous to the cooling flow occurring in galaxy clusters. A simple expression for the infall rate is given by:

$$\dot{M}_{cool} = 4\pi \rho_{gas} r_{cool}^2 \frac{dr_{cool}}{dt}. \quad (11)$$

Note that for small halos (that we find preferentially at early times), the cooling radius is greater than the virial radius, and we are in the *cold mode* regime, where equation 10 applies. At late

times, for large values of the virial velocity, the cooling radius falls below the virial radius and we are in the *hot mode* regime. As a consequence, at high redshift we have a more efficient cooling. Hydrodynamical simulations, such as that of Kereš et al. (2005), justify the use of two different modes of cooling. Indeed, they found that a cold mode dominates for low-mass objects, that are found at high redshift or in low-density environments in the nearby universe, while the hot mode contributes significantly for high-mass systems, therefore being important only at low redshift. Anyway it is worth to note that in our model the cooling at high redshift might be enhanced due to the assumption of a constant metallicity. In case of a metal-dependent cooling rate we would obtain a lower cooling in the high redshift objects with primordial metallicity. We will test such effect in a future version of the code, where the chemical evolution model will be implemented.

3.3. Galaxy Sizes and Angular Momentum

Since several time-scales involved in the analytic treatment of galaxy formation (such as for example the star formation rate) that we are going to introduce in the following sections depend on the dynamical time of the galactic disc ($t_{dyn} = r_{disc}/v_{disc}$), it is important to have an accurate description of their sizes. The disc size will depend on the virial radius of the halo where the galaxy was born, and on its angular momentum. Indeed, if the halo is asymmetric and surrounded by a clumpy distribution of matter, then it can acquire an angular momentum from a net tidal torque. To quantify the angular momentum of the system, one often refers to the spin parameter, which is a dimensionless quantity, defined as:

$$\lambda = \frac{J|E|^{1/2}}{GM_{halo}^{5/2}}, \quad (12)$$

where J , E and M_{halo} are the total angular momentum, gravitational binding energy and mass of the halo. The distribution of the spin parameter as found in N-body simulations (Warren et al. 1992; Cole & Lacey 1996) can be approximated with a log-normal distribution with $\langle \lambda \rangle = 0.05$ and $\sigma_\lambda = 0.5$. Hereafter we will assume the mean value for λ . Mo, Mao, & White (1998) related the disc radius to the spin parameter and to the virial radius assuming that the angular momentum of the disc is a fixed fraction of that of the halo:

$$r_{disc} = \frac{1}{\sqrt{2}} \left(\frac{j_d}{m_d} \right) \lambda R_{vir}, \quad (13)$$

where m_d is the ratio between the disc mass and the halo mass, and j_d is the ratio between the angular momentum of the disc and of the halo. Higher values for the spin parameter result in larger discs, because they contract less before reaching the centrifugal equilibrium. The above relation holds in the case of halos approximated with isothermal profile and neglecting the gravitational effects of the discs themselves, but the authors also give the correct expression in the case of NFW profiles and self-gravitating discs. As shown by Mo, Mao, & White (1998), it is a reasonable assumption to take $j_d \approx m_d$, which gives us:

$$r_{disc} = \frac{\lambda}{\sqrt{2}} R_{vir}, \quad (14)$$

which leads to galactic discs that are over an order of magnitude less extended than their halo hosts. Under the assumption that we are considering negligible the self-gravity of the disc, the disc circular velocity is equal to the halo virial velocity.

The assumption that the specific angular momentum of the disc is the same of that of the halo, as implied by $j_d \approx m_d$, leads to disc sizes that well match the observed spirals (Mo, Mao, & White, 1998), hence it became the standard assumption of disc modelling. Nevertheless, hydrodynamical simulations find that the gas loses most of its angular momentum during accretion, producing discs too small compared to that observed (Navarro & White, 1994). It is still unclear if this effect is simply due to the limited mass resolution employed, or to the absence of some form of feedback.

3.4. Star Formation

Obviously, the physical processes governing the rate with which the (primordial) gas is transformed into stars play a critical role in models of galaxy formation. Unfortunately, they are still subject to major uncertainties, given the extremely complex interplay of phenomena on the largest (magnetic fields, gas angular momentum, etc.), as well as smallest (radiative cooling, thermal conduction, dust extinction, etc.) scales. Nevertheless, observations indicate the existence of some useful laws to describe SF on global scale, larger than star-cluster scales. Analysing a large sample of spirals and starburst galaxies, Kennicutt (1998) found two empirical correlations for the star formation per unit area, Σ_{SFR} : (i) $\Sigma_{SFR} \propto \Sigma_{gas}^{1.4}$ and (ii) $\Sigma_{SFR} \propto \Sigma_{gas}/t_{dyn}$. These empirical estimates justify the use of parametric forms for the star formation prescription in semi-analytical models, where the star formation time-scale is given by the dynamical time.

In our model we consider two modes of star formation. In the first one, the *quiescent mode*, the star formation rate is simply assumed to be proportional to the amount of cold gas available and inversely proportional to the time-scale of star formation, that is assumed here to be the dynamical time of the disc: $t_{dyn} = r_{disc}/v_{disc}$. The efficiency of the star formation process is quantified by the free parameter α_{quie} defined by the relation:

$$\dot{M}_* = \alpha_{quie} \frac{M_{cool}}{t_{dyn}}. \quad (15)$$

Since this gas is assumed to share the same high value of the angular momentum as previously discussed, stars formed in this way are added to the disc component of the galaxy.

The second mode of star formation considered in GECO is the *burst mode*. Starbursts are allowed to occur after a merger between galaxies, that can be due to the cannibalism of a satellite galaxy by the central one or to a collision between satellites. Indeed, a strong correlation between galaxy interactions and starburst activity is observed both in the present-day universe and at high redshift. This is for example the case for ULIRGs, the Ultra-Luminous Infrared Galaxies discovered locally by IRAS and then found in large numbers at high- z by ISO and Spitzer, exhibiting the most violent episodes of star formation (Kennicutt, 1998; Sanders & Mirabel, 1996). The assumption of a starburst triggered by a galaxy merger is furthermore justified by several numerical simulations (Mihos & Hernquist, 1994, 1996), that show how, during the merger phase, gas sinks to the central region of the galaxy and the increased density leads to an enhanced level of star formation (according to the Kennicutt law). Recent simulations (Cox et al., 2008) indicate that the starburst event can be triggered in the major, as well in the minor, mergers, but with an efficiency which strongly depends on the galaxy mass ratio (as implemented also in Somerville, Primack, & Faber 2001; Menci et al. 2004).

Therefore, in our model, the star formation during the starburst is given by:

$$\dot{M}_* = f_{burst} \frac{M_{cold}}{t_{burst}}, \quad (16)$$

where t_{burst} is the dynamical time of the largest disc, while f_{burst} is the efficiency of the burst, assumed to be linearly proportional to the merger mass ratio:

$$f_{burst} = \beta_{burst} \frac{m_1}{m_2}, \quad (17)$$

where m_1 and m_2 are, respectively, the smallest and the biggest galaxy, and β_{burst} is a free parameter. Stars formed in such way are added to the bulge component of the galaxy.

In addition to the increased rate of star formation, major mergers between spirals move stars from circular orbits to random motions, hence producing a remnant that generally resembles an elliptical galaxy. For these reasons, we can safely assume that after that kind of mergers, the discs previously present in the colliding systems are transformed in a spheroid. We define a merger to be a major one when $\frac{m_1}{m_2} > 1/3$. Spheroid formation through disc instability is not considered in the present work.

3.5. Feedback Processes

Feedback processes are mechanisms which regulate the efficiency of star formation. The need for some form of feedback in low-mass halos, which suppresses cold gas accretion, was first recognised by White & Rees (1978), in order to flatten in some way the faint-end of the luminosity function, which turned out to be too steep compared to the observational data available at the time. SN feedback and photoionization are commonly considered to reduce the faint-end slope.

Although initially the motivation for invoking feedback was to suppress cooling, and hence star formation, in low-mass halos, in recent years the focus was shifted to attempt reproducing the bright-end of the luminosity function, which in the most classical models resulted in an excess of bright objects at low redshift compared with the observations (again a manifestation of the basic problem to shape an essentially power-law form for the DM mass function into a Schechter exponential function for the baryons). Although the behaviour of the cooling function implies that the cooling time increases in high-mass halos, this is not enough to explain the sharp observed cut-off in the galaxy luminosity or stellar mass functions, and some mechanisms preventing the cooling rate in high-mass halos is also needed (and is commonly identified in the AGN effect, see below).

3.5.1. SN feedback

The first form of feedback considered in our model is that from SN explosions and high-mass stars outflows, which eject gas and energy into the surrounding Interstellar Medium (ISM). This is supported by several evidences of Supernova driven winds in dwarf star-forming galaxies (Martin, 1999; Strickland et al., 2000; Heckman, 2001), which also suggests that the gas reheating rate is proportional to the SFR.

The parametrisation of the SN feedback is based on simple energy arguments. The rate of reheating will be proportional to the SFR, to the number of Supernovae per solar mass of stars, given by $\eta_{SN} = 4 \times 10^{-3} M_\odot$ for a Salpeter Initial Mass Function (IMF), to the energy released by each SN, about $E_{SN} = 10^{51} \text{ ergs}$, and to the efficiency with which the SN energy

is transferred into the ISM, ϵ_{SN} . This last parameter is highly uncertain, and is usually treated as a free parameter. The rate of reheating will be more efficient for galaxies living in low potential wells. In order to mark the depths of the potential well of the host halo, we use the halo circular velocity, so that the rate of reheating will be simply proportional to V_c^{-2} . This implies that galaxies living in low-mass halos are affected by SN feedback effects, and their star formation will be self-regulated, while in high-mass halos this kind of feedback is ineffective. The rate of reheating will be finally given by:

$$\dot{M}_{heat} = \epsilon_{SN} \frac{4 \eta_{SN} E_{SN} \dot{M}_*}{5 V_c^2} \quad (18)$$

(Kauffmann, White, & Guiderdoni, 1993; Somerville & Primack, 1999).

The reheated gas is removed from the cold gas reservoir, and can not be used to form new stars. We assume an *ejection* model of feedback, that means that the reheated gas is ejected from the halo and is unable to cool until it is reincorporated into a more massive halo at the following step of the merging hierarchy. Although our re-incorporation scheme assumes a fast fallback (analogous to the fast re-incorporation of De Lucia et al. 2004), we found that it produces better results compared to the *retention* model, in which the gas can subsequently cool. In particular we obtain a better match of the faint-end of the stellar mass function.

3.5.2. Reionization

It is now known that the hydrogen in the intergalactic medium (IGM), that became neutral at $z \sim 1000$, must have been ionized at later epochs, although the redshift at which this reionization occurred is still quite uncertain, ranging from $z = 6$, as imposed by the lack of a Gunn-Peterson trough in quasar spectra at that redshift (Fan et al., 2000), up to $z = 11$, as imposed by the constraint on the optical depth to the last scattering surface measured from WMAP5 data.

If a large population of galaxies and quasars exist at very high redshift, as predicted by galaxy formation models and confirmed up to $z \sim 6$ by observations (Fan et al., 2000), then reionization could have occurred through photoionization, since both young galaxies and quasars emit UV photons, able to ionize the IGM. This photoionizing background may also act to inhibit galaxy formation in two ways. It can heat the IGM, increasing the thermal pressure of the gas and preventing it to collapse into the dark matter halos. The second way is through a reduction of the cooling rate of gas inside halos, mainly reducing neutral atoms which can be collisionally excited. This results in a strong suppression of galaxy formation in low-mass halos.

According to previous studies (Thoul & Weinberg, 1996; Gnedin, 2000; Somerville, 2002), after reionization the above mechanisms prevent gas accretion in halos with $V_c < 50 \text{ km s}^{-1}$, with the result that galaxy formation is strongly suppressed in such systems. Hence, in our model, we mimic the effect of photoionization by suppressing gas cooling in halos having a circular velocity lower than that at redshifts greater than the redshift of reionization, assumed to be $z_{re} = 6$. Although the exact value of the redshift at which reionization starts is still uncertain and other models treat it as a free parameter, we realized that by varying its value our results does not change appreciably and we choose to fix it. This is in agreement with previous works that found that the properties of the galaxy population are almost insensitive to the assumed redshift of reionization (Kravtsov, Gnedin, & Klypin, 2004; Macciò et al., 2009).

Indeed, at very high redshift the leaves of the tree have very small mass and the only cooling mechanism is the H_2 cooling, which is very inefficient.

The simple approach used in our model for the reionization were demonstrated by Benson et al. (2003) to have very similar effects to the self-consistent treatment of the photoionization described, for instance, in Benson et al. (2002). In Appendix B we present the effect of varying the assumption on the limit of the circular velocity.

3.5.3. AGN feedback

There is growing evidence for a tight relationship between galaxy evolution and the growth of super-massive black holes (SMBHs) powering nuclear activity. Supporting evidences come from the tight correlations between the BH mass and the mass of the bulge (Häring & Rix, 2004) and that between the black hole mass and the velocity dispersion of stars in the bulge (Ferrarese & Merritt, 2000; Gebhardt et al., 2000). The mutual feedback between galaxies and quasars may be the reason for such strong correlations.

We implement the accretion onto black holes in our model following the prescriptions of Kauffmann & Haehnelt (2000) and Croton et al. (2006). We allow two different modes of feedback, one following the starburst triggered by galaxy mergers and strong interactions, the *quasar mode*, and a second one, the *radio mode*, taking place at low rate during the whole life of the galaxy. A third natural way of growth for SMBH's is represented by the coalescence of the BHs residing in the centre of two merging galaxies. In this case, after the merger of the host galaxies, the new BH mass is simply the sum of the two progenitors. We thus simplify our treatment by ignoring the occurrence of BH binary systems and gravitational wave losses of angular momentum.

We use as a starting point a seed mass for the BH in the galaxies on the bottom of hierarchy, i.e. living in the “leaves” halos. These seeds are believed to form at very high redshift, but it is quite unclear if they formed from the direct collapse of pre-galactic gaseous discs or if they are the remnants of massive Population III stars (Volonteri, Lodato, & Natarajan, 2008). We take a seed mass equal to $1000M_\odot$, and checked the consequence of this choice by using different mass values: the results do not depend on this choice, at least for small values of the seed. Since we start placing the seeds at the bottom of the hierarchy, the redshift at which they are planted depends upon the time at which the leave haloes fall below the mass resolution of the tree and it can be higher than the redshift of the reionization. Anyway, they can not grow before the reionization starts since gas accretion, that is the main mechanism of feeding BHs, is inhibited.

The first mode of accretion is motivated by the observations of bright AGN and quasars radiating with high efficiency, close to their Eddington limit. It is widely believed that this mechanism of accretion is triggered by galaxy mergers, since they can drive rapid inflow of gas toward the centre of the galaxy, feeding both the starburst and the BH.

As in Kauffmann & Haehnelt (2000), we assume that during a merger of galaxies a certain fraction of cold gas is accreted on to the centre of the black hole:

$$\dot{M}_{BH}^{QSO} = \frac{f_{BH} M_{cold}}{1 + (280 \text{ km s}^{-1}/V_c)^2} \Delta\tau^{-1}, \quad (19)$$

where f_{BH} is an efficiency parameter to be chosen in order to match the relation between black-hole mass and velocity dispersion of the bulges and $\Delta\tau$ is the time interval of the integration

of differential equations. In this way QSO accretion is closely linked to the starburst activity of the galaxy, which is triggered by galaxy mergers together with BH accretion, naturally producing BH masses proportional to the mass of the spheroidal component that is formed only during the starburst.

The second way of accretion, the radio mode, is a continuous and quiescent accretion during the whole life of the galaxy, during which the black-hole accretes gas directly from the hot halo. This is supported by observations of radio galaxies (mainly in high-density environments, like groups or clusters of galaxies), which are accreting at a sub-Eddington rate, hence in a rather inefficient fashion. In spite of this inefficiency, the energy extracted from the BH accretion in the form of collimated jets is believed to contrast the cooling flow in the centre of clusters. Assuming that in this case the BH is fuelled with a Bondi accretion rate, the resulting BH growth rate is given by (Croton et al., 2006; Somerville et al., 2008):

$$\dot{M}_{BH}^{RADIO} = k_{AGN} \frac{M_{BH}}{10^8 M_\odot} \frac{f_{hot}}{0.1} \left(\frac{V_c}{200 \text{ km s}^{-1}} \right)^3, \quad (20)$$

where f_{hot} is the ratio between the hot gas mass and the halo mass and k_{AGN} is a free parameter, with the dimensions of an accretion rate ($M_\odot \text{ yr}^{-1}$).

The most important channel building up the mass of the black hole is the *quasar mode*, in which the accretion rate can be much greater than the Eddington luminosity. The second way of accretion, the *radio mode*, provides negligible contribution to the present-day black-hole masses, being several order of magnitude below the Eddington rate. Nevertheless this is an important source of feedback in high mass halos, as it suppresses cooling flows as well as the quasar mode mechanism, and it occurs for whole life of the galaxy, while the *quasar mode* acts only in a very short period of the galaxy life. The feedback efficiencies of such processes, very difficult to model *a-priori*, are set by trying to match various observables. The efficiency of the *quasar mode* accretion is set by requiring the model to match the $M_{BH} - M_{bulge}$ relation, while the *radio mode* accretion efficiency is tuned to optimize the shape of the stellar mass function, and in particular the observed knee at the characteristic stellar masses.

The injection of energy into the ISM due to the presence of an AGN is modelled in the following way. The mechanical heating generated by the the black hole accretion is given by

$$L_{BH} = \eta \dot{M}_{BH} c^2, \quad (21)$$

where c is the speed of light and η is the global efficiency of energy production close to the event horizon in nuclear black-holes, and is set to the reference value of 0.1. The gas cooling rate in the halo is then corrected by this energy injection according to:

$$\dot{M}_{cool}^{new} = \dot{M}_{cool}^{old} - \frac{L_{BH}}{V_c^2/2}. \quad (22)$$

To avoid an unphysical negative value for the cold gas accretion rate, we enforce mass conservation by assuming an amount of newly formed cold gas mass in the time-step $\Delta\tau$ the maximum between zero and $\dot{M}_{cool}^{new} \Delta\tau$, where \dot{M}_{cool}^{new} is given by eq. (22). Hence, the cooling rate can not only be reduced, but even stopped in the case of a strong BH accretion rate.

3.6. Galaxy Dynamics

During the merger of two dark matter halos, the baryonic cores that they contain, being more compact and less subject to tidal

effects, may avoid merging with each other, and end up orbiting within the new combined halo. An halo formed by many mergers may contain many distinct galaxies, with the galaxy in the most massive halo becoming the central galaxy and all the others becoming the satellites. These satellite galaxies gradually lose their energy and angular momentum under the action of dynamical friction until they sink to the centre of the halo and merge with the central galaxy. Moreover, they are subject to random gravitational collisions that can occur with other satellites.

3.6.1. Dynamical Friction

The effect of dynamical friction in slowing down the orbital velocities of galaxies moving through a sea of dark matter particles was originally described by Chandrasekhar (1943) and previous SAM made use of this approach. Although early N-body studies (Navarro, Frenk, & White, 1995) gave support to the merger time-scales predicted by the classical approach, recent numerical and hydrodynamical simulations (Jiang et al., 2008; Boylan-Kolchin, Ma, & Quataert, 2008) have shown that the Chandrasekhar's approach underestimates the merger time-scale for minor mergers and overestimates it for major merger events. As an estimate of the dynamical friction timescale we have assumed the fitting formula of Jiang et al. (2008), derived from hydro/N-body simulation:

$$t_{df} = \frac{0.94\epsilon^{0.6} + 0.6}{2C} \frac{M_{halo}}{m} \frac{1}{\ln(\Lambda)} \frac{R_{vir}}{V_c}, \quad (23)$$

where C is a constant equal to 0.43, $\ln \Lambda$ is the Coulomb logarithm, that can be approximated to $\ln \Lambda = \ln(1 + M_{halo}/m)$, ϵ is the circularity parameter of the satellite's orbit, given by $\epsilon = J/J_c$, with J the angular momentum of the actual orbit and J_c the one of the circular orbit with the same energy. We adopt the average value found in numerical simulations: $\langle \epsilon \rangle = 0.51$ (Tormen, 1997; Jiang et al., 2008).

It is worth noting that the time-scale increases as the halo mass increases, so that at high redshift, when the halos are less massive, we find an high rate of merging, whereas it decreases at low redshift, where we have an accumulation of sub-halos inside the parent halo.

An important consideration concerns the mass m used to compute the dynamical friction time-scale. As soon as a galaxy becomes a satellite in a larger halo, its initial mass is determined by its total (dark matter and baryonic) mass. However, as it shrinks towards the centre, a large fraction of the dark halo is stripped away, while the mass of the gaseous core is too dense to be stripped. Thus, the effective mass of the satellite decreases with time and the dynamical friction time-scale should increase. We realized that, by neglecting this effect, the time-scales for merging were too small, leading to an overmerging, particularly at low redshifts. We have taken into account the effect of tidal stripping allowing the mass of satellite varying with time according to the time-scales predicted by Taffoni et al. (2003). Hence we assume that the satellite loses their dark halo 1.5-2 Gyr since entering the virial radius (for simplicity here we are neglecting the tidal stripping on the baryonic core, hence we do not consider tidally destroyed satellites).

3.6.2. Satellite Collisions

In addition to the mergers driven by dynamical friction, we include random collisions between satellites. We consider for the satellite encounters the cross-section of Mamon (1992), which is

a simplified version of that derived from N-body simulations by Roos & Norman (1979). The resulting merger rate is given by:

$$k = 2 \sqrt{\pi} \alpha_p^2 \alpha_v R_{vir}^2 v_{gal} K(V_c/v_{gal}), \quad (24)$$

where v_{gal} is the internal dispersion of the satellite galaxy, V_c and R_{vir} are the circular velocity and virial radius of the host halo, respectively, $\alpha_p = 4$ and $\alpha_v = 5.4$ are dimensionless parameters, while K is a dimensionless merger rate given by:

$$K = \left[\frac{1}{x} + \frac{2}{x^3} - \frac{2 \exp(-x^2)}{x^3} - \frac{3 \sqrt{\pi} \operatorname{erf}(x)}{2 x^2} \right] \quad (25)$$

$$x = \frac{\alpha_v v_{gal}}{2V_c}. \quad (26)$$

For realistic values of the ratio V_c/v_{gal} the merger rate decreases with this ratio and becomes very low for galaxy clusters. Given the merger rate we can compute the collision time as:

$$t_{coll} = \frac{1}{kn}, \quad (27)$$

where n is the number densities of galaxies in the halo. We obtain shorter merger time-scale at high redshift, when the number density of galaxies is higher. The probability for having a merger for a satellite with another one, randomly chosen, will be $P = \Delta t/t_{coll}$, where Δt is the lifetime of the halo. We consider only binary mergers, and we assume that such event occurs when $P \geq 1$. During a collision between two satellites we allow a burst of star formation in the same way as the one occurring during a merger between a satellite and the central galaxy. The effect of including such process, in addition to the mergers involving the central galaxy due to dynamical friction, is to decrease the fraction of low-mass galaxies in favour of intermediate-high mass objects, hence to slightly modify the shape of the galaxy mass function.

3.6.3. Remnant

After the merger, the total mass of the remnant (dark matter and baryons) is the sum of the two merging galaxies, while the new radius and circular velocities are computed from applying the conservation of energy and the virial theorem. According to the virial theorem, the total internal energy is given by $E_{int} = -T$. By applying the conservation of energy:

$$T_{new} = T_1 + T_2 - E_{orb}, \quad (28)$$

where T denotes the kinetic energy and E_{orb} is the mutual orbital energy:

$$E_{orb} = -f_{orb} \frac{Gm_1m_2}{r_1 + r_2} \quad (29)$$

(r_1 and r_2 are the radius of the two progenitors and f_{orb} is a parameter which weakly depends on the density profile, we assume $f_{orb} = 2$). These considerations yield to:

$$R_{new} = \frac{(m_1 + m_2)^2}{m_1^2/r_1 + m_2^2/r_2 + f_{orb}m_1m_2/(r_1 + r_2)}. \quad (30)$$

In the case of major mergers involving two equal galaxies ($m_1 = m_2$ and $r_1 = r_2$) the size of the remnant is a factor of 4/3 greater than the initial size.

Table 1. Free parameters

Parameter	Meaning	Best-fit value	Range
α_{quiet}	star formation	0.01	0.01-0.1
β_{burst}	burst efficiency	0.68	0.5-1
ϵ_{SN}	SN feedback efficiency	0.5	0.01-1
f_{BH}	AGN feedback efficiency in QSO mode	0.006	0.001-0.1
k_{AGN}	AGN feedback efficiency in radio mode	1×10^{-6}	$10^{-7} - 10^{-6}$

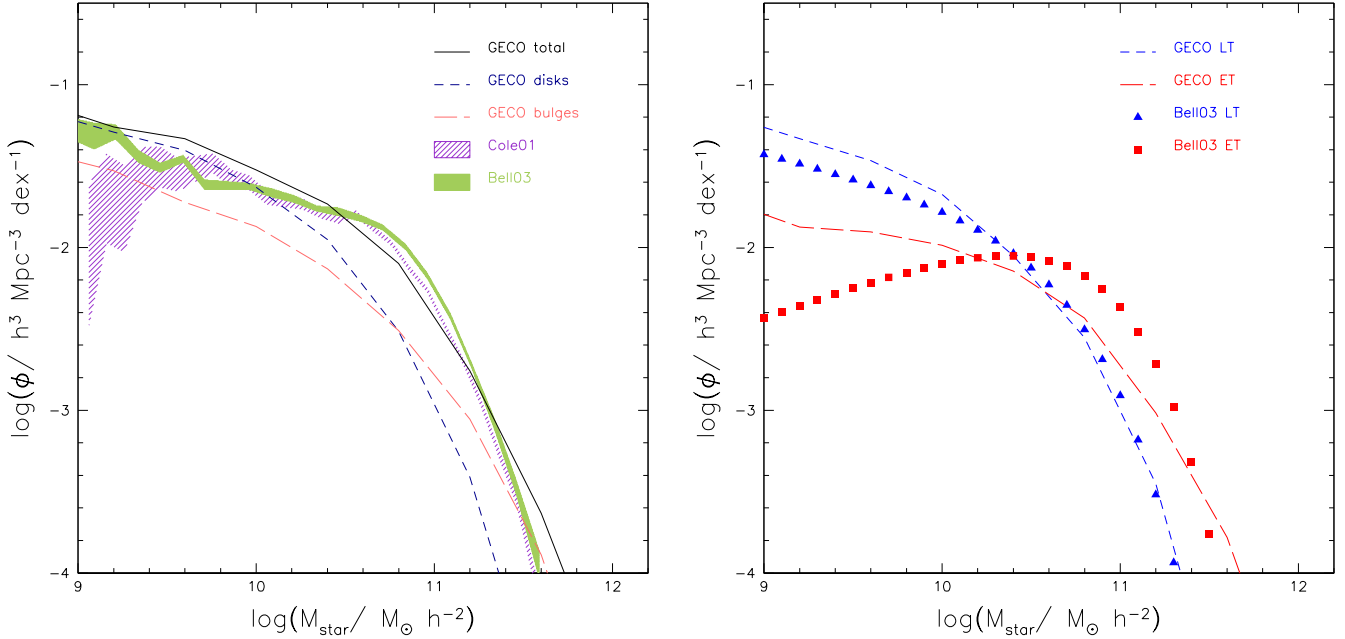


Fig. 2. Left panel: Stellar mass function at $z=0$. Black solid line represents the SMF resulting from GECO, purple shaded region stays for the C01 observed mass function with its error-bar, and the green shaded one from B03. Also shown is the contribution to the total stellar mass content from bulges (red long dashed line) and discs (blue short dashed line). Right panel: Stellar mass function at $z=0$ of early-type (red long dashed line) and late-type galaxies (blue short dashed line) compared with the observed one by B03: red squares for early-type and blue triangles for late-type.

3.7. Galaxy Morphology

In our model the morphology of a galaxy is determined by the relative importance of the bulge over the disc component. The only way of formation for discs is through the quiescent mode of star formation, while bulges can grow in two ways: through star formation occurring in a starburst event, hence triggered by any event of merger, and through the disruption of discs following a major merger. In this case all the stars belonging to the discs undergoing a merger are added to the bulge of the remnant galaxy. Such galaxy may eventually form a new disc if some fraction of cold gas is still present.

We can assign a crude morphological type to each galaxy by using the ratio between the bulge mass and the total stellar mass: $r = M_{bulge}/M_{star}$. Using the prescription of Bertone, De Lucia, & Thomas (2007), we classify as Ellipticals galaxies with more than 70% of their stars in bulge, as Spirals galaxies having $0 < r \leq 0.7$, and as Irregulars galaxies without any bulge.

4. Setting the free parameters

In the previous section we have introduced several free parameters in the analytical prescriptions which model galaxy formation. In summary they are:

1. α_{quiet} : efficiency of star formation in quiescent mode
2. β_{burst} : efficiency of star formation in starbursts
3. ϵ_{SN} : efficiency of SN feedback
4. f_{BH} : efficiency of AGN feedback in the *quasar* mode
5. k_{AGN} : efficiency of AGN feedback in the *radio* mode

We will first infer constraints on their values by comparing the model results, obtained for a large grid of parameter values, with observations of the local universe. In particular we focus on the build-up of the stellar mass, and we require our model to fit the local stellar mass function, as well as the relationship between the black-hole mass and the bulge mass. The stellar mass function is obviously influenced by all the parameters together. The star formation efficiency in the quiescent mode α_{quiet} affects the overall shape and normalisation of the function; ϵ_{SN} affects the faint-end (or low-mass end); β_{burst} determines the contribution of the bulge on the total stellar content, and we require that at the bright-end bulges dominate over discs. The AGN efficiencies, f_{BH} and k_{AGN} shape the bright-end of the mass function.

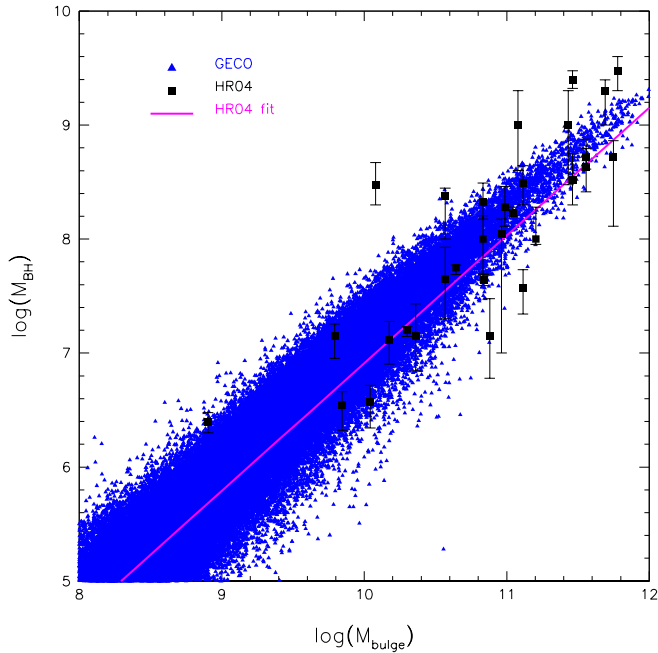


Fig. 3. Black-hole versus bulge mass relation at $z=0$. Blue triangles represent data for modelled galaxies, while black squares with error-bars are data from Häring & Rix (2004). The magenta solid line is their best fit relation.

Moreover, the AGN efficiency in the *quasar* mode, i.e. the one triggered by the starburst episode, determines the relationship between the mass of the black-hole and the bulge mass, affecting mainly the normalisation of the relation, while the slope turns out to be very close to the one observed almost independently on the value of this efficiency, since in the model the growth of BHs and bulges are closely linked. In Table 1 we report the value of these parameters in our best-fit model and the allowed range. Unless otherwise stated, in the following we always will refer to this best-fit model.

5. Matching data from the local universe

A key observable for comparing predictions of any models of galaxy formation is the number density of galaxies as a function of their stellar mass in the local universe, the stellar mass function (SMF) at $z = 0$. We will use it to constrain our model free parameters. We refer to two measurements of the local SMF. The first is that reported by Cole et al. (2001), hereafter C01, obtained by combining data from the Two Micron All Sky Survey (2MASS) and the 2dF Galaxy Redshift Survey. The second estimate, by Bell et al. (2003), exploited a large sample from 2MASS and the Sloan Digital Sky Survey (SDSS). We choose to show their g -selected sample (taken from their table 5). Both estimates use near-infrared data to compute stellar masses and hence are highly reliable. All data are transformed to a Salpeter IMF.

In the left panel of Figure 2 we show the stellar mass function at $z = 0$, resulting from the model and compared with the C01 and B03 observations. The model is able to reproduce with good accuracy the shape and normalisation of the SMF, especially in the bright-end ($M_{star} > 10^{11} M_{\odot} h^{-1}$). Compared to the C01 mass function, the model shows a slight excess of

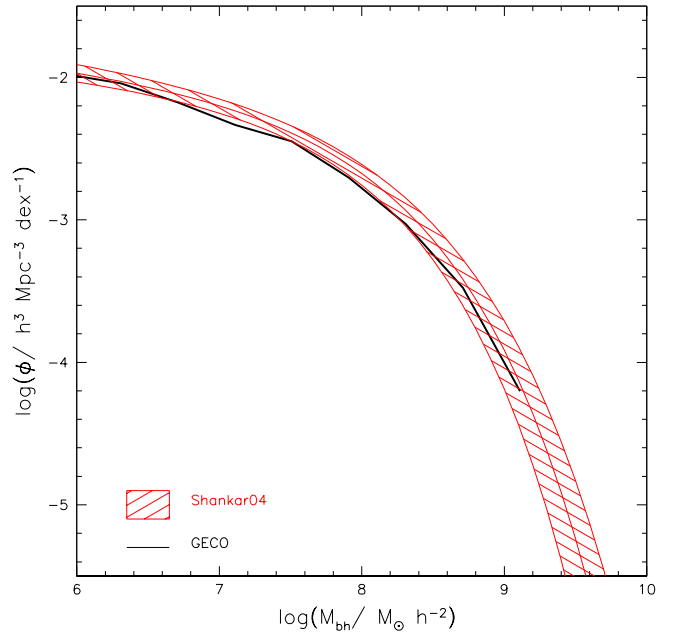


Fig. 4. Local Black-hole mass function of the model (black solid line) compared with the estimates of Shankar et al. (2004) (red shaded region).

galaxies at the faint-end. However, the B03 estimate presents a steeper faint-end, resulting in closer agreement with our prediction. Our model also shows an underestimation of galaxies at the knee of the mass function ($10^{10.5} - 10^{11} M_{\odot} / h^2$), an effect already present, for instance, with the Millennium galaxy catalogue (Bertone, De Lucia, & Thomas, 2007). Such dearth may be partly explained with the combined effect of SN and AGN feedback that are both effective in this mass range. Moreover, since the deficit is due to a lack of intermediate-mass early-type galaxies, (see right panel of Fig. 2) it is likely connected to the excess of low-mass spheroids, as satellite galaxies are not able to become massive enough in the model for the reasons described later in this section.

It is worthwhile to stress the fundamentally different shapes of the halo mass and the luminous (stellar) mass functions presented here. The general shape of the dark matter halo mass function (see Figure 1), as predicted by any theoretical models based on hierarchical dark-matter clustering, is a pure power-law with a steep faint-end and no knee at the high masses. A turn-off mass does exist, but it occurs at much higher masses ($M \sim 10^{15} M_{\odot}$) than the characteristic one observed in the stellar mass function. In order to obtain a Schechter shape for the mass function, many effects contribute. At the faint-end side, the feedback from SN and from the photoionization background suppresses star formation in small halos, hence reducing the faint-end slope. At the bright-end, the difference between the exponential cut-off observed in the stellar mass function and the power-law shape expected for the halo mass function is explained with the inter-play of various independent effects. On one hand, there is a marked dependence of the gas cooling on the halo mass: the cooling time decreases with the halo mass. In addition, the two modes of gas cooling discussed in Sect. 4.3 have an halo mass dependence: in the *cold mode* regime the gas accretes towards the centre in a time-scale given by the free-fall

time, while in the *hot mode* regime the accretion rate is governed by the cooling time, and is much less efficient than in the former case. Since in high-mass halos the accretion mainly occurs through this last mechanism, this may explain why in this halos gas is not able to cool efficiently. Moreover, the AGN feedback acting on this scales, further reduces the cooling, leading to an approximately correct number of massive galaxies.

In Figure 2 (left panel) the separate contributions to the total stellar content from discs and bulges are also shown, as blue short-dashed and red long-dashed lines, respectively. As expected, the bright-end is dominated by bulges, meaning that objects with very high-mass ($M_{star} > 10^{11} M_{\odot} h^{-1}$) do not essentially contain discs, that have been presumably destroyed during a major merger. On the contrary, discs overcome the number densities of bulges at low masses, and start to be dominant in the mass range $M_{star} \sim 10^{10.5} M_{\odot} h^{-1}$. Note that this value is close to the transition mass, $\sim 3 \times 10^{10} M_{\odot} h^{-1}$ at $z=0$, at which a transition in several galaxy properties is observed (Kauffmann et al., 2003) and where early-type galaxies start to dominate over the late-type ones in the local universe (Baldry et al., 2004; Bundy, Ellis, & Conselice, 2005).

So far we have considered only the contribution to the total stellar mass density from the disc and bulge components. In the right-end panel of Fig. 2 we show the mass function of early-type and late-type galaxies. As defined in the previous Sect., early-type galaxies are defined as galaxies whose bulge makes at least 70% of the total stellar mass. We include in the definition of late-type systems both spiral and irregular galaxies. We compare the predicted mass function with the results of B03. With this definition of morphologies, the agreement with the observational data is quite good, in particular we accurately reproduce the transition mass at which the number density of ellipticals/S0s equals that of late-type galaxies locally. Anyway, we note quite a large excess of faint early-type galaxies with masses below $10^{10} M_{\odot} / h^2$. This is a long-standing problem that afflicts all the SAMs in the recent literature (Weinmann et al., 2006; Croton et al., 2006; Cattaneo et al., 2008; Somerville et al., 2008) and may be regarded as an indication of a wrong treatment of the satellite population. A common way among SAMs of treating the satellites is to assume that the hot gas in a system that merges into a more massive one is instantaneously stripped (strangulation) and added to the reservoir of the new central galaxy. As a consequence, the star formation in the new satellite is quenched shortly once it has consumed its cold gas. This crude treatment of the strangulation is clearly an oversimplification and recent hydrodynamical simulations indicate that such a process occurs on a larger time-scale, of the order of 1-10 Gyr (McCarthy et al., 2008), allowing the star formation to continue for some time after the coalescence, hence lowering the fraction of red satellites (Kang & van den Bosch, 2008). Although even tidal disruption (see for instance Somerville et al. 2008) can help in decreasing the faint-end, it is unlikely that it can change the relative number of early and late-type satellites (Kimm et al., 2009). Other effects, such as the ram pressure on the cold gas in the galaxy (Lanzoni et al., 2005) may also play a role in the formation of the satellite population and should be included in the future SAMs.

In order to set the efficiency of black-hole growth, we require our model to match the observed relation between the black-hole mass and the mass of the stellar bulge in the local universe. Since the major channel for the growth of black-hole is given by the accretion during the *quasar* mode triggered during a starburst event, where all the stars formed are added to the bulge component, it comes with no surprise that black-hole and bulge are closely linked. Nevertheless, in order to obtain an acceptable fit, where

both the slope and the normalisation of the relation are well reproduced, some fine tuning of the f_{BH} and k_{AGN} parameters were required.

In Figure 3 we show the comparison between our derived relation (blue triangles) with data from Haring & Rix (2004), represented by the black squares with error-bars, and their best-fit relation, shown by the magenta line. The observed relation is well reproduced by our model over the whole mass range (note in any case that the Haring & Rix (2004) fit is derived only for bulge masses $M_{bulge} > 10^{10} M_{\odot}$). Anyway, the scatter in the model results to be smaller than that observed, as the model neglects the contribution to the bulge formation due to disk instabilities, and the only channel to build spheroids is through mergers, hence directly linked to the BH formation.

A further test performed on the black-hole population is shown in Figure 4, where we show the BH mass function of the model, compared with the local estimate by Shankar et al. (2004). The remarkable agreement between the observed and predicted BH number densities, together with the well matched BH-bulge relation is encouraging and suggests that our method of implementing AGN feedback, though simple, is accurate enough.

6. Comparing GECO with high-redshift galaxy statistics

Having obtained in the previous Sect. a good match of GECO's predictions with the global properties of galaxies in the local universe, it is instructive now to attempt a first comparison of the evolutionary properties of the model with the galaxy statistics in the distant universe, with no further adjustment of the model parameters. Given the wide range of physical processes included in GECO, one would expect at least a rough agreement of the global properties, unless some key physical processes might have been overlooked.

6.1. The Evolution of the Stellar Mass Function

We first test the resulting mass function with observations up to $z \sim 3.5$. A comparison of the GECO's mass functions with those observed is reported in Figure 5. Here we match our model mass functions with results from Franceschini et al. (2006), hereafter FR06, Fontana et al. (2006), hereafter F06, Pérez-González et al. (2008), PG08, Marchesini et al. (2009), M08 and Berta et al. (2007), B07. All data are transformed to a Salpeter IMF. We consider only mass function estimates which take into account IRAC bands in the stellar mass derivation, since the lack of Spitzer data in the near-IR leads to an overestimation of the stellar masses at $z > 3$ (see F06). Note that error-bars in FR06 take into account only Poisson statistics, hence resulting to be much smaller than in the other data, where uncertainties in photometric redshifts, stellar masses and cosmic variance are considered.

Considering the spread between different estimates of the mass function, the comoving number density of massive galaxies in our model is roughly consistent with the observed values, although with a tendency to underpredict the data, especially at high redshifts. In the highest redshift bin considered ($z \sim 3.5$), the bright-end is marginally consistent with that of F06 but systematically lower than M08 and PG07. Note however, that including the effects of different assumptions in the Spectral Energy Distribution (SED) modelling leads to different MF estimates fully consistent with each other (see M08).

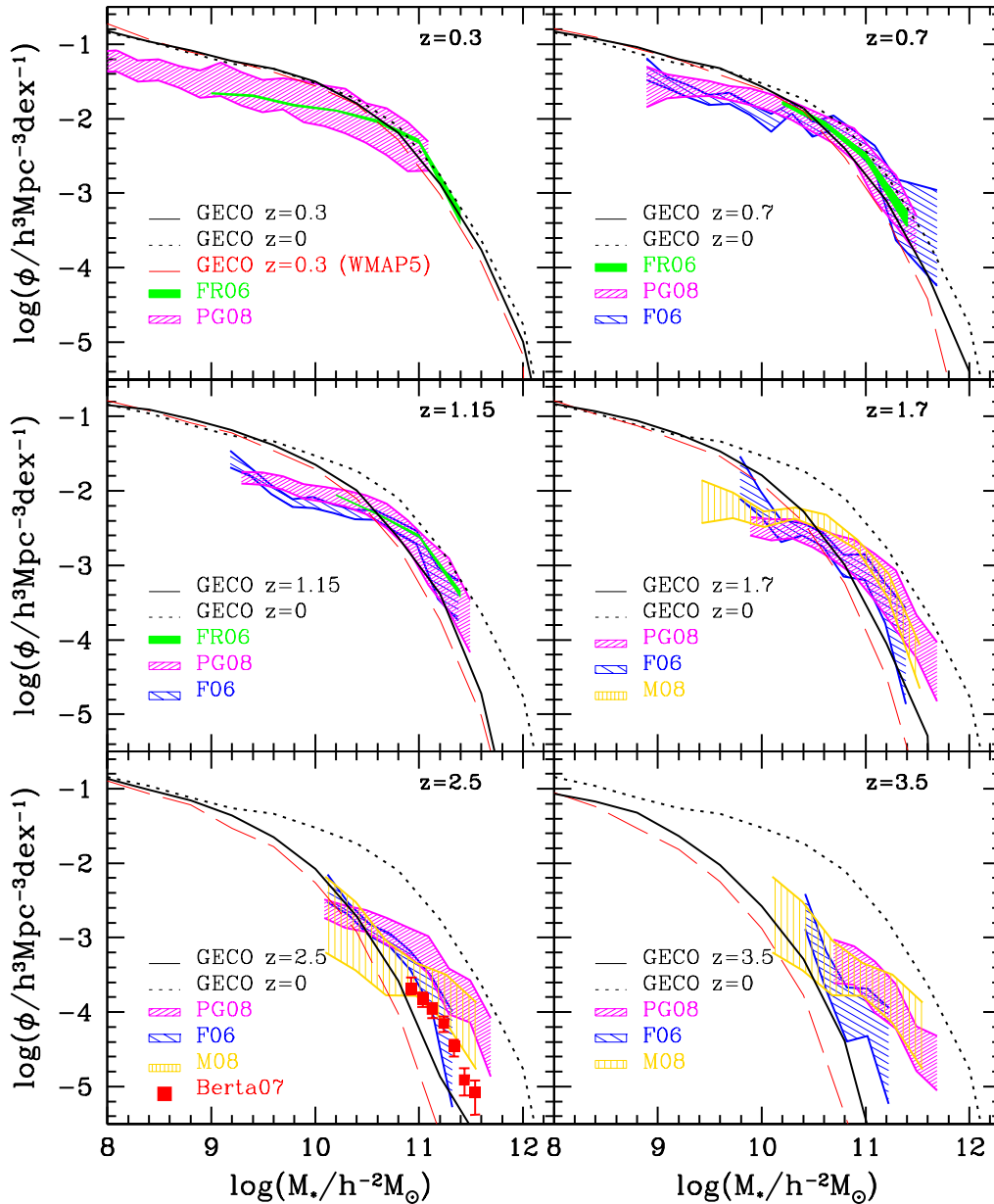


Fig. 5. Comparison between GECO’s mass functions at high redshift, up to $z \sim 3.5$. The green shaded region indicates the mass function of Franceschini et al. 2006, the magenta one is that of Pérez-González et al. 2008, the blue region is the estimate of Fontana et al. 2006, the yellow shading is from Marchesini et al. 2009 and the red squares at $z \sim 2$ show the results from Berta et al. 2007. GECO predictions are represented with a solid black line. The dotted line in all the panels is the GECO mass function at $z = 0$, reported as reference and the red dashed line is the model prediction for the WMAP5 cosmology.

A remarkable feature in the comparison of model expectations with the data concerns the faint end of the mass function, where the model tends to keep systematically in excess of the observed number of low-mass objects at any redshifts: whereas there is a significant evolution in the number density of low mass galaxies in the data, the model predicts modest or no evolution up to redshift of one. The mismatch between data and hierarchical models at the faint-end seems a common feature among different models (Fontana et al., 2006; Fontanot et al., 2009; Monaco et al., 2009).

In the same figure 5 we also include the predictions for the SMF adopting the WMAP5 set of parameters indicated by the red dashed line. The main difference with the Concordance cosmology is a lower value of σ_8 and a tilt in the primordial power spectrum ($n < 1$), implying a delay in the formation of structures. Indeed, this is observed in the evolution of the SMF, where, at high redshift the model predicts a later assembly of galaxies, exacerbating the underproduction of massive galaxies at higher redshifts.

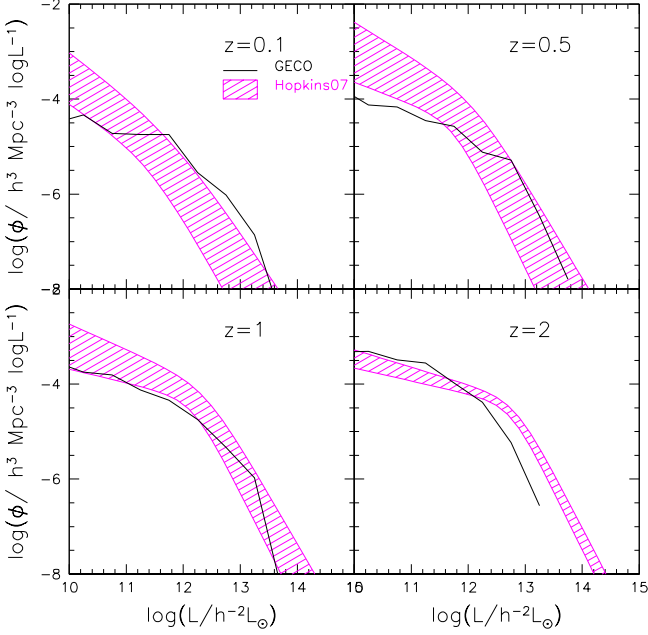


Fig. 6. Comparison between GECO’s quasar luminosity functions at different redshifts and observations by Hopkins, Richards, & Hernquist 2007. The magenta shaded region indicates the quasar luminosity function of Hopkins, Richards, & Hernquist 2007, while GECO predictions are represented with a solid black line.

It is worth to note, however, that such a comparison must be taken with caution before deriving firm conclusions. The errors in the stellar mass estimates can strongly affect (in the sense of increasing) the counts in the bright-end where the mass function is very steep. An improved approach would be to convolve the model stellar mass function with the error distribution in the stellar mass given by the observations (Kitzbichler & White, 2006; Stringer et al., 2009; Cattaneo et al., 2008). Of course the uncertainties in the stellar mass estimates increase with redshift and this can influence the amount of the observed evolution of the stellar mass function.

Finally, it is not unlikely that the derivation of the stellar mass function at the faint-end might have been seriously influenced by incompleteness effects in the source selection and have produced a spurious evolution at low masses. More extensive deep imaging by Spitzer will be carried out on large areas during the warm mission phase, which will offer an opportunity to address these issues shortly.

6.2. Quasar luminosity function

The gas accretion onto black holes described in Sect. 3.5.3 triggers the AGN activity whose bolometric luminosity associated is given by L_{BH} (eq. 21). Although the accretion rate in our model is not limited by the Eddington rate, we limit the quasar luminosity to lie below this limit:

$$L_{QSO} = \max(L_{BH}, L_{Edd}). \quad (31)$$

In order to test the consistency of the feedback from AGN activity on the galaxy population we compare the quasar luminosity function predicted by GECO with observational estimates. To avoid to introduce further uncertainties due the obscuration fac-

tor in the optical bands, we compare our predictions with bolometric luminosity functions. We refer to the compilation from Hopkins, Richards, & Hernquist (2007), obtained by collecting a large multi-wavelength dataset, from the optical, soft and hard X-ray, near- and mid-IR. The authors give obscuration-corrected luminosities, aimed to represent the intrinsic quasar population. In Figure 6 we show our predicted quasar luminosity function up to $z=2$. The model gives an acceptable description of the evolving quasar population at low and intermediate redshift, but at higher redshift (panel at $z=2$) it underpredicts the number of luminous quasars. Varying the efficiency of the accretion onto black hole (f_{BH} and k_{AGN}) does not solve the problem, because the match at high redshift would be obtained at the expense of the agreement of the local black-hole mass function. This may be an indication that the parametrisation of the AGN activity used in the present work is not completely adequate, as already suggested by Marulli et al. (2008), and an accretion efficiency increasing with redshift may be required (as suggested even by recent hydrodynamical simulations, see Viola et al. 2008), to fit simultaneously the low and the high redshift luminosity function (Marulli et al., 2008; Lapi et al., 2006). We also suggest that higher accretion efficiencies at high redshift may be reached also with an enhanced cooling efficiency at early times. This alternative may also provide a way to form galaxies more efficiently at high redshift, hence, improving the match of the stellar mass function evolution.

6.3. Formation Histories of the Stellar Populations

In order to get a deeper insight into the process of the stellar build-up in our modelled galaxies, we investigate here their detailed star formation histories (SFH). We derive the SFH *a-posteriori* for each present-day galaxies, taking into account its baryonic tree and summing up all the stellar populations formed inside its progenitors. We compute the SFHs over 52 time-steps, our pre-defined grid of times used for the merger tree. We show in Figure 7, as an example, the SFHs for 4 different realizations of the central galaxy of a halo with mass $5 \times 10^{12} M_{\odot}$, i.e. very similar to the Milky-Way halo. We indicate the stars formed in the quiescent mode with a blue shaded histogram and with the red one the stars formed during the starburst phase. The black envelope is the sum of both contributions. In each panels, the host halo mass and stellar mass are indicated, together with the parameter r , that is the ratio between the bulge and the total stellar mass.

In the case of such a Milky-Way-like halo, the majority of the central galaxies are spirals ($\sim 60\%$). However, the mix of galaxy properties turned out to be rather heterogeneous. In the lower-right panel we see an example of quite smooth star formation history with a steep rise of SFR at early times followed by a smooth decrease. In the two upper panels we see that more than one peak of quiescent star formation are present, indicating that star formation has occurred in different progenitors of the final galaxy. In other cases, the starburst can occur at more recent times ($z \lesssim 0.5$ in the lower-left panel) and is more efficient in consuming all the gas, hence the galaxy evolves passively until present. In all the cases represented starburst events are very frequent at early times, even in galaxies that at the present time have a late-type morphology.

In order to give an indication of the age of a galaxy, we define its formation redshift as the redshift when the galaxy has formed half of its present-day stellar mass. We indicate it in Fig. 7 as a vertical dashed line. Galaxies with a smooth, quiescent star formation tend to form their stars later, while galaxies having

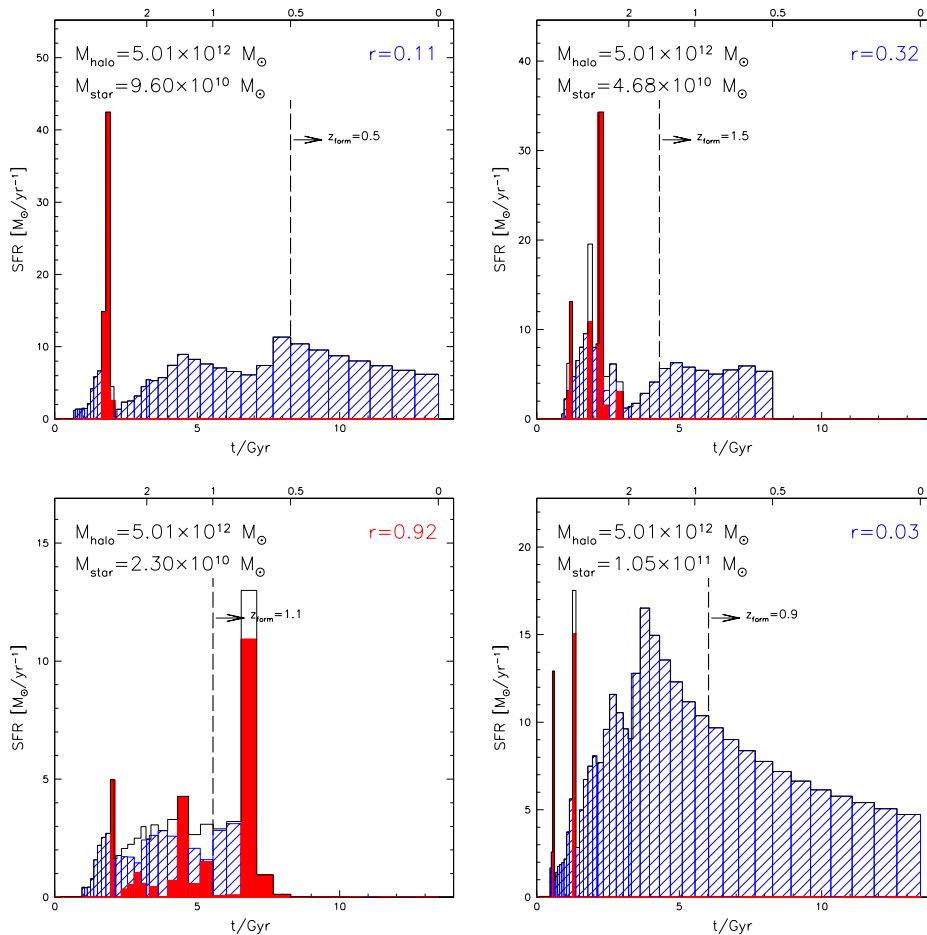


Fig. 7. SFHs of stellar populations for different realizations of the central galaxy of a Milky-Way like halo, having masses equal to $5 \times 10^{12} M_{\odot}$. These SFHs sum up the contributions to the final galaxy stellar mass by all the stars present in the galaxy at $z=0$. Blue shaded histograms show the star formation occurring in the quiescent mode, the red ones represent the bursty mode, while the black envelope is the total SFR. The vertical dashed line indicates the formation redshift of the galaxy. The final stellar masses in each realizations are indicated.

experienced a more bursty star formation history, thus having an elliptical morphology, tend to have higher formation redshifts.

In Figure 8 we show the SFH of the central galaxy of halos with different mass, averaged over 100 realizations of the same parent halo tree. Halo masses range from $\sim 10^{11} M_{\odot}$ up to $\sim 10^{14} M_{\odot}$. Note that, while in Fig. 7 the SFHs refer to single realizations of one halo, each panel here refers to the average over 100 realizations of the same halo, hence SFHs result to be smoother. Two trends with the halo mass can be noticed. The first is that, passing from low-mass to high-mass halos, the starbursts become the dominant mechanism of star formation. The second is that the star formation rate for galaxies living in high-mass halos peaks at higher redshift compared to that in lower mass objects. Therefore, the associated formation redshift for massive objects is higher. In fact, the increasing importance of the starburst mode, together with the AGN feedback connected to it, lead to a fast consumption of gas at early times, by preventing the gas to cool and inhibiting further star formation. The consequence is a lower rate of star formation at later times, hence higher average formation redshifts for galaxies living in high-mass halos.

Since high-mass galaxies live in high-mass halos, these results indicate that stars in massive galaxies are on average older

than in their less massive counterparts. Nevertheless even in massive galaxies the star formation is not completely quenched, but a long tail of star formation at low redshift still occurs. This behaviour of our SFHs appears to be in general agreement with the evidence for a *downsizing* pattern of galaxy evolution, an effect discussed since long time (Cowie et al., 1996; Gavazzi & Scodeggio, 1996; Franceschini et al., 1998; Thomas et al., 2005). We will discuss further the physical reasons for this in Sect. §7.

6.4. The Cosmic Star Formation Rate Density

The evolution of the comoving star formation rate density for the whole galaxy population is shown in Figure 9 (left panel). The model prediction is shown by the black line and is compared with data from the compilation by Hopkins (2004), for UV, optical and radio tracers, and from Rodighiero et al. (2009) for the IR tracers. Different colours encode different tracers for the SFR: cyan for star formation derived from the UV continuum, green for optical tracers (O_{II} , $H\alpha$ and $H\beta$), magenta for data using radio tracers and red for SFR estimates derived from the IR luminosity. The latter are believed to offer particularly reliable and robust estimates of the star-formation rate because

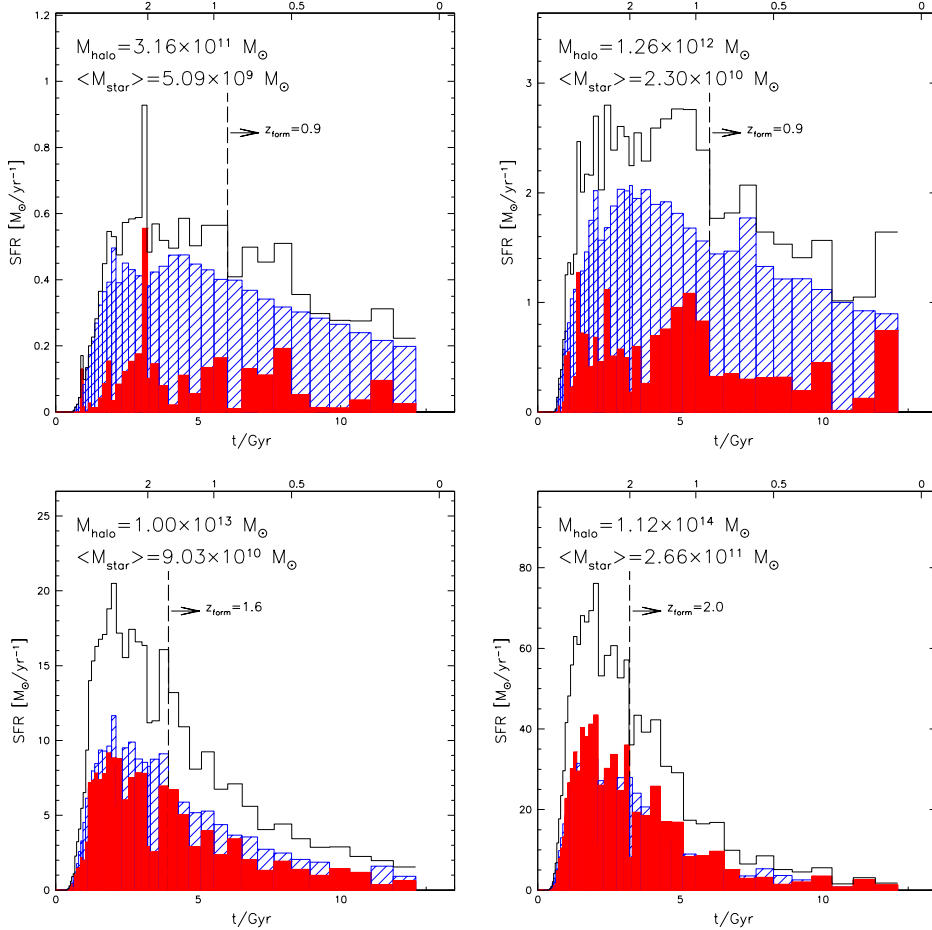


Fig. 8. Averaged SFHs for central galaxies of 4 different halos, with masses ranging from $\sim 10^{11} M_{\odot}$ to $\sim 10^{14} M_{\odot}$. The average are computed over 100 realizations. As in figure 7, blue shaded histograms show the star formation occurring in quiescent mode, the red ones represent the bursty mode, while the black envelope is the total SFR. The host halo mass and the averaged final stellar mass are indicated.

they trace rather directly the emission by young stellar populations and are free of dust extinction effects (Kennicutt, 1998; Franceschini et al., 2001; Elbaz et al., 2002). The blue star at $z \approx 7$ is the determination of the SFR density of Bunker et al. (2009) through HST-WFC3 data with the z' -drops technique, effective over the redshift range $6.7 < z < 8.8$, as indicated by the x-axis bar.

The model provides a remarkably good fit to the data over most of the redshift range. It should be stressed, in particular, the nice agreement of the model with IR data, showing a fast rise from $z = 0$ to $z = 1$ and then a wide plateau up to $z \sim 4$. Locally ($z \lesssim 0.2$) there is an indication that our model produces too many stars. It appears consistent with UV determinations, but it keeps higher with respect to the determination of Rodighiero et al. (2009) using the Spitzer $24\mu\text{m}$ luminosity function. Even at very high redshift ($z \approx 7$), the model is marginally consistent with the observations, especially if we take into account that the HST-WFC3 data can be considered as a lower limit due to incompleteness effects. We note also that the WMAP5 model predicts a much lower SFR at high redshift, ($z \geq 2$) leading to a better agreement with the $z \approx 7$ data. Contrary to what found in Somerville et al. (2008), with the new cosmology we find a better agreement with data in the SFR density, but a worst one in the stellar mass assembly, as noted above.

The high level of star formation rate at redshifts $z \approx 3 - 5$ found in the model was already mentioned in the previous Sect. On one hand, the quiescent mode of star formation is very effective, due to the high cooling efficiency in denser environment. Indeed, the peak in the quiescent mode of star formation (blue shaded histograms in Figs. 8) is always at $z \sim 2$. On the other hand at high redshift the star formation mainly occurs in starbursts, triggered by the high merging rate, which enhances the SFR at early cosmic times. The exhaustion of cold gas available explains the sharp later decline at lower redshifts.

In the right panel of Figure 9 the contribution to the total star formation rate density (black solid line) is splitted according to the mass of the hosting halo: the short-dashed red line shows the contribution from galaxies living in high-mass halos ($M > 3 \times 10^{12} M_{\odot}$), while the green long-dashed line shows the one from galaxies living in less massive halos. The time dependence of the star formation rate in the two cases has a similar behaviour: a slow increase at high redshifts, a phase of peak activity, and finally a quick decline to the present time. However, in addition to this general pattern, we notice a systematic shift in the SFR history between the two halo populations, with the high-mass halo activity being shifted at higher redshifts, $z \sim 2 - 4$, while it is more concentrated around $z = 1 - 2$ in the less massive population.

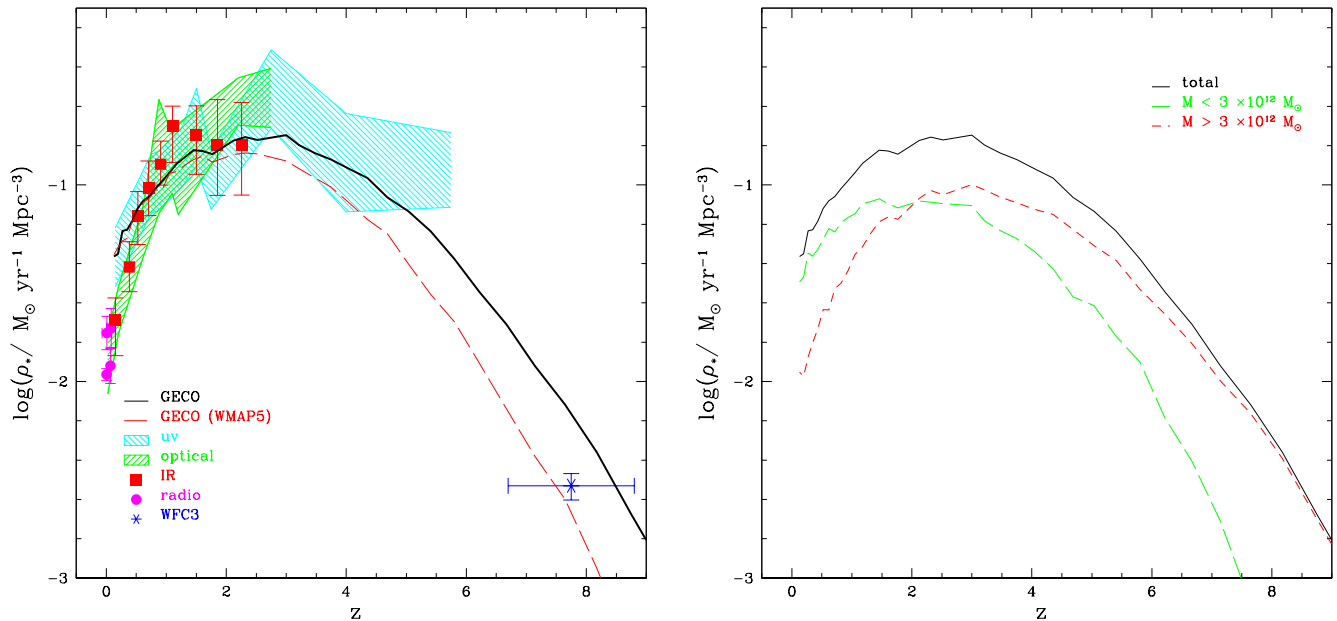


Fig. 9. Left panel: SFR density as a function of redshift. Solid black line shows the GECO predictions. The shaded area and coloured points are the SFR obtained from observations at different wavelengths. The cyan shaded region shows the SFR derived from UV tracers, green region means that observations are in the optical, and magenta dots in the radio (from the compilation of Hopkins 2004); red squares refer to infrared determinations, from Rodighiero et al. (2009) and the blue star is the $z \simeq 7$ determination from HST-WFC3 data (Bunker et al., 2009). Right panel: SFR density splitted in the contribution by objects residing in different halo masses. Solid black line shows the total SFR density, red short-dashed shows the contribution from galaxies living in high-mass halos ($M_{\text{halo}} > 3 \times 10^{12} M_{\odot}$), while the green long-dashed curve represents the contribution from galaxies in less massive halos ($M_{\text{halo}} < 3 \times 10^{12} M_{\odot}$).

We then confirm our previously found results: galaxies residing in high-mass halos form their stars at earlier epochs, and then their star formation rapidly slows-down, while galaxies in less massive systems form stars at an enhanced rate even at recent times ($z \lesssim 1$).

6.5. Star Formation and Mass Assembly

We have discussed in the previous Sect. an important aspect of our model, its prediction that massive systems form their stars at earlier times than less massive objects. This however concerns the birth times of the galaxy’s stellar populations, while the times of mass assembly may be very different when stars are formed at high redshift in a number of distinct progenitors and are assembled at more recent times.

In Figure 10 we compare the star formation history with the “assembly history” for single realizations of various parent halos. In the upper boxes of each panel we show the SFH of all stellar populations contributing to the final galaxy, in analogy with those reported in Fig. 7. The SFH is expressed here in terms of the fraction of the final stellar mass formed in each time-step (instead of the SFR), for an easier quantitative comparison with the assembly history. In the bottom boxes we show the mass assembled into the main progenitor at each time-step, where the main progenitor identifies at each redshift the progenitor of the galaxy which survives until the present day. Here, red histograms indicate the amount of stars added to the bulge in a given time-step, while blue histograms show the stars added to the disc. Although in a few cases the history of stellar assembly is very similar to that of star formation, indicating that star formation took place

mainly in one single object, in general the two paths may be significantly different.

In most of the cases the assembly of bulges, due to mergers, is related to starbursts, although in some systems, mainly in merging episodes at low redshifts, the mass assembly is not associated to any event of star formation because the gas content is already consumed (*dry merging*). Substantial dissipationless merging may lead to very different formation times for the process of star formation and mass build-up. Although dry mergers in the local universe are observed, their frequency and their role in galaxy evolution are still poorly constrained by observations (van Dokkum, 2005; Bell et al., 2006). Anyway galaxy formation models predict that they are a crucial process in the formation of local ellipticals (see Cattaneo et al. 2010).

We define the redshift of assembly as that corresponding to when half of the final stellar mass is assembled in one single object, and we show it in Fig. 10. By definition, the assembly redshift is always smaller than the formation one, they equal each other when almost all the stars are formed in the main progenitor.

We report in Figure 11 the dependencies of the mean star formation redshift (upper panels) and the redshift of mass assembly (lower panels) as a function of the hosting halo mass (left-hand panels) and of the galactic stellar mass (right-hand panels). Error-bars indicate the standard error of the mean over 100 MC realizations of the same host halo. Note that in order to derive the redshift of formation (or assembly) as a function of stellar mass we weight each galaxy mass by the number density of its host halo, because any stellar mass may belong to a certain range of halo masses.

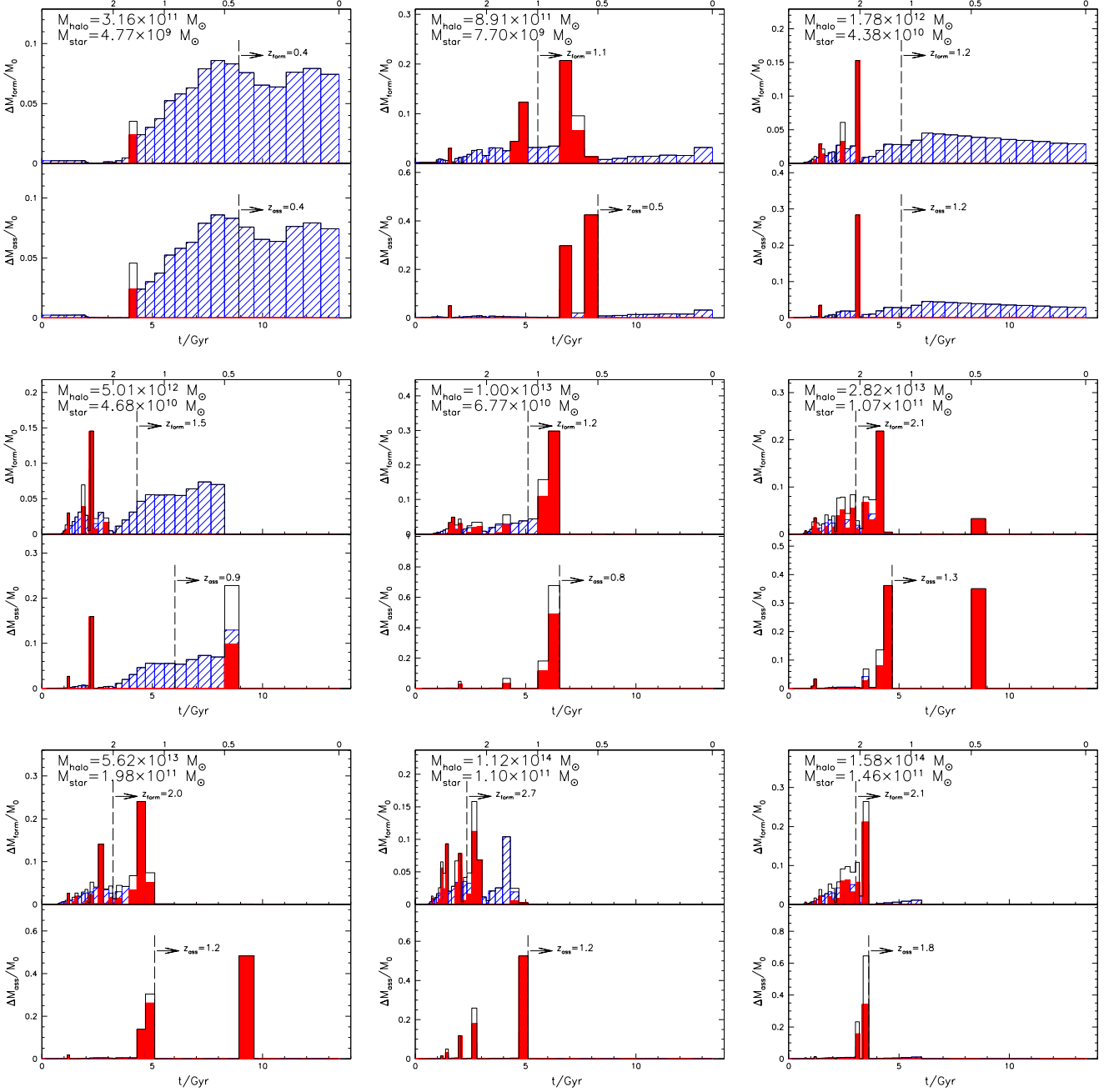


Fig. 10. Comparison between stellar mass formed (upper panels) and assembled into the main progenitor (lower panels) for different model galaxies, living in different halos. In the upper panel red and blue histograms represent, respectively, bursty and quiescent SF, while in the assembly panels red and blue stay for the mass assembly of bulges and discs respectively.

The mean formation redshift shows a clear increase with both halo and stellar mass. This effect is more pronounced for the central galaxies than for the whole population including satellites. We have already shown in the previous Sects. how galaxies living in high-mass halos formed their stars earlier and at a faster rate than in low-mass halos. Here, we demonstrate that the trend is true even with the galactic stellar mass, although it is weaker. Note that the most massive halos ($M_{halo} > 10^{14} M_{\odot}$) host galaxies with the higher formation redshift ($z_{form} \sim 2.5$, top left panel of the figure), but since these halos are very rare, the mean formation redshift of the more massive galaxies ($M_{star} \sim 10^{12} M_{\odot}$),

which belong to a certain range of halo masses, keeps somewhat lower (~ 2 , top right panel).

The behaviour of the redshift of mass assembly is more difficult to interpret. We found that, on average, galaxies living in high mass halos assemble their stars earlier. Indeed, the merger time-scales due to both dynamical friction and random collisions among satellites increase with the halo mass. We already mentioned in §3.6.1 that the dynamical friction time increases with the ratio between the mass of the halo and that of the satellite (eq. 23). Moreover, since the merger probability is strongly reduced in high-velocity encounters, the merger rate for satellites decreases with the ratio V_c/v_{gal} (eq. 24), and becomes very low

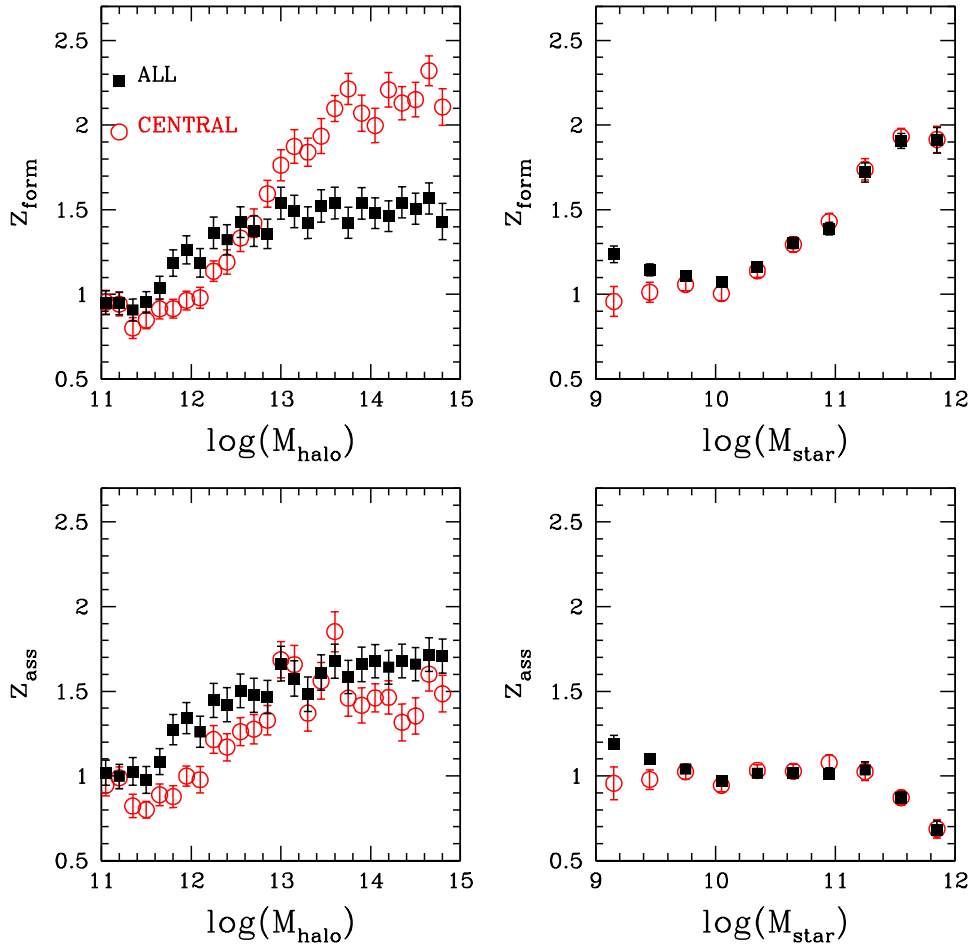


Fig. 11. Mean formation redshift (upper panels) and assembly redshift (lower panels) of galaxies as a function of their host halo mass (left-hand panels) and stellar mass (right-hand panels). Black squares indicate the global population of galaxies, including central and satellites, while red open circles stay for central galaxies. Error-bars indicate the standard error on the mean over 100 MC realizations of the same halo.

for massive cluster-size halos. Nevertheless, when the redshift of mass assembly is expressed in terms of the galactic stellar mass, the downsizing behaviour is no more recovered: the assembly time keeps approximately constant around $z_{\text{ass}} \sim 1$ for low and intermediate masses and decreases in the highest mass end, with $z_{\text{ass}} \sim 0.7$ for $M_{\text{star}} \sim 10^{12} M_{\odot}$. These stellar mass values correspond to those of the CD galaxies in local rich clusters or groups. The combined effects of the formation redshift and the assembly redshift suggest that the only way to form the most massive galaxies in the local universe is in the form of dry mergers at recent times. Indeed, massive galaxies cease to form stars quite early and, without such events, they are not able to grow their mass above $M_{\text{star}} \simeq 10^{11} M_{\odot}$.

In conclusion, our model expectation is that, although mergers and collisions are rare in massive halos, they do happen, and their effect is crucial in the formation of the today most massive galaxies. Refined observational estimates of the galaxy mass functions at the high mass-end all over the $z=0$ to 4 redshift interval (on top of those already apparent in Fig. 5) will clarify how far this expectation of a substantial *dry merging* process is born out by the data.

7. Discussion and Conclusions

We have presented a new semi-analytical model of galaxy formation, the Galaxy Evolution Code, GECO which appears to reproduce several key statistical properties of local and high-redshift galaxies.

GECO is based on a state-of-the-art Monte Carlo algorithm for the representation of the dark matter halo merging history, based on the Extended Press-Schechter formalism. GECO includes detailed implementations for gas cooling, star formation, feedback from SN and galaxy mergers, due to both dynamical friction and random collisions. Moreover, the parallel growth of BHs is followed in time and the subsequent AGN feedback is modelled.

We specifically tested our results directly on the observables involving the stellar mass and star-formation rate more than luminosities, as usually done by other published models. This is motivated on one hand by the fact that the stellar mass functions are the most direct outcome of the model. On the other hand, stellar masses in galaxies have recently become a rather straightforward observable thanks to rest-frame near-infrared data by the Spitzer Space Telescope, directly probing the stellar mass content in high-redshift galaxies. At the same time, Spitzer is also

probing with deep far-infrared photometric imaging the rate of stellar formation in distant objects. Therefore, we can compare the outcomes of our model with the most reliable set of observables and a minimal number of free parameters. We thus believe that the basic physics of the Λ CDM hierarchical clustering concept of galaxy formation can be tested by us in a very effective way.

The main results obtained in the present work are summarised in the following.

1. The local stellar mass function results in a remarkably good agreement with the determination of Cole et al. (2001) and Bell et al. (2003) (Fig. 2). At the high-mass end the total mass function is dominated by the contribution of bulges, while discs dominate at the faint-end. When the total stellar mass is splitted into the contributions of early-type and late-type galaxies, the former populate the bright-end side, while the latter mainly contribute at low masses. The number densities of the two morphological types cross each other at $M_{star} \sim 3 \times 10^{10} M_{\odot} h^{-1}$, as observed. Although we reproduce the general trend of the morphological mass functions, our model fails in matching the low-mass end of spheroids, showing an excess of low-mass systems. Likely, this is due to an oversimplification of the satellite population, since satellite galaxies lose their hot gas reservoir as soon as they are incorporated in a more massive halo and the star formation is quenched soon after.
2. The co-evolution of galaxies and BHs is modelled following the prescriptions of Croton et al. (2006). A first mode of accretion onto BHs considered is the so called 'radio-mode', that inhibits the quiescent star formation, while the second one is the 'QSO-mode', that is triggered only during galaxy mergers and constitutes a major channel of BH accretion. As a consequence of mergers, a starburst is induced as well, feeding the galactic bulge component (and destroying the disc in the case of a major merger). This leads to a parallel growth of BH and bulges with the two masses very well correlated, in agreement with observational data (Haring & Rix, 2004) and to the local black-hole mass function in a remarkable agreement with the observations of (Shankar et al., 2004).
3. We compare the stellar mass functions resulting from the model with various observational determinations up to $z \sim 3.5$ (Fig. 5) and found a reasonably fair agreement over the whole redshift range considered. Nevertheless, the observed ratio between the evolution of the faint- and the bright-end of the stellar mass function is not very accurately reproduced: there is too much evolution in the model at the bright-end and too little at the faint-end compared to observations. Various sets of observables indicate a large increase in the number density of low-mass objects between $z \sim 2$ and the present-day and a lower rate of evolution for massive objects. However, we mentioned that the completeness and robustness of the observational mass function are to be proven there, before claiming more definite conclusions. In the case of WMAP5 cosmology we observe a delay in the formation of cosmic structure, that lead to a further reduction of high-mass systems.
4. The bolometric quasar luminosity function is compared with Hopkins, Richards, & Hernquist (2007), showing a good level of agreement at low and intermediate redshift, but a tendency to underpredict the number of bright quasars at high redshift. A mechanism for enhancing the cooling rate at high redshift might simultaneously increase the fuel for BHs and enhance the SF at high redshift, as seems to be required to improve the match with the stellar mass functions.
5. The integrated star formation rate density (Fig. 9) shows an high level of star formation at high redshifts, a peak at $z \sim 1.5 - 3$ and then a sharp decline below $z \sim 1$. When compared with the determination of the SFH derived using various tracers (UV, optical, radio, IR), our predictions are in very close agreement with these observations. At very high redshift ($z \simeq 7$) our model is able to correctly reproduce the recent determination of the SFR density by HST-WFC3 data.
6. We analysed in detail the SFH in simulated sets of galaxies, to gain insights into how the model treats star formation and how it depends on the galaxy or halo mass. We computed the averaged SFH for the central galaxies living in halos of different sizes (Fig. 8). We identified two main trends with halo mass. First, going to high-mass systems, the contribution of the starburst mode to the total SF becomes increasingly important, and indeed predominant in very high mass objects. Second, the formation redshift, defined as that when half of the present-day stellar mass is formed, increases, leading to older stellar populations in massive systems. Hence galaxies in our model form their stars following a *downsizing* pattern, consistent, for instance, with the dating of stellar populations in local galaxies (Thomas et al., 2005). The naive expectation of early versions of hierarchical galaxy formation models was that, since massive halos are assembled later than their lower-mass counterparts, the most massive galaxies, hosted in the largest halos, should form their stellar content at the same late cosmic time. Actually, as shown in Fig. 11, this is clearly not the case in our refined model. According to it, *downsizing* in star formation is an intrinsic feature of semi-analytical models (see also Neistein, van den Bosch, & Dekel 2006). The present-day massive galaxies were formed through the assembly of a number of smaller progenitors, that collapsed at high redshifts from the highest density peaks of the primordial density field. According to this scenario, also named biased galaxy formation (Dekel & Silk, 1986), bright and massive systems started to form stars early on. This feature is a natural outcome of the merger tree formalism: progenitors of high-mass halos fall below the resolution mass imposed to the merger tree after several time-steps back in cosmic time, so the leaves of the tree are found at high redshift. On the contrary, smaller systems, closer to the resolution mass, take only a few time-steps back to reach this minimum mass. Note that this is not merely a computational artifact, but indeed corresponds to the fact that we expect quite negligible star formation to have occurred below such threshold mass, on consideration of the SF quenching by the UV photoionizing background (Sect. 3.5.2). Since baryons are put into halos starting from the leaves, in high mass halos star formation took place at early times. Moreover, at high redshift both mechanisms of star formation were more effective. Thanks to the efficient cooling of the gas, the quiescent mode of star formation occurs at enhanced rate. Also, the frequency of mergers at these times is high, allowing an efficient conversion of gas in stars via a starburst. The exhaustion of cold gas is, therefore, very rapid, leaving the galaxy devoid of fuel, and preventing further star formation to occur. A further reason for the star formation quenching in massive systems may be ascribed to AGN feedback. In order to check the importance of such mechanism, we run a test simulation with the AGN emission switched off. The comparison between the two versions of the model are presented

in Appendix A. We found that AGN feedback has some effect in increasing the average age of stellar populations in the most massive galaxies, as it was pointed out by previous works (Croton et al., 2006; De Lucia et al., 2006; Cattaneo et al., 2008). However, in our model the *downsizing* trend is still obtained, although slightly weaker, even in the absence of an AGN.

Therefore, in GECO, the AGN feedback has not a dramatic effect in producing the local galaxy properties (see also Menci et al. 2006 and Monaco, Fontanot, & Taffoni 2007) and it is not the main reason for the *downsizing* pattern of galaxy evolution. In our modelling, the latter is rather due to a higher efficiency of SF back in time for the most massive galaxies in rich environments, as explained above. Although we have shown that the *downsizing* is quite a natural feature of our model, it is not the case for all the published models and some of them fail in reproducing such trend with mass, as it is shown in Fontanot et al. (2009).

7. Finally, we compared the star formation history of simulated galaxies with the mass assembly history, that is the history of the mass assembled into the main progenitor at each time-steps (Fig. 10). As expected, the two processes may occur on very different time-scales, especially in high-mass systems, where the star formation took place at high redshift in many distinct progenitors, which assemble at low redshift. The late assembly of these systems occurs in the majority of the cases through *dry mergers*, i.e. mergers between spheroidal systems with little or no gas. In these cases, the merger is not accompanied by any event of star-formation, neither quiescent nor bursting. An intriguing question is then whether galaxies in the model assemble their stellar mass in a *downsizing* way, as it occurs for the star formation. Possible downsizing effects in the mass assembly were indicated by several authors (Bundy et al., 2006; Cimatti, Daddi, & Renzini, 2006; Hopkins et al., 2007) as inferred from the lack of evolution in the high-mass end of the mass function and by the evolution of the blue-to-red galaxy crossover mass (the mass for which the early-type mass function intersects that of late-types). In our model, we found that although the assembly time shows a shallow dependence on the host halo mass, on average galaxies living in massive halos assemble their stars before galaxies in less massive hosts (Fig. 11). Instead, the assembly times are almost constant with stellar mass, and decrease for very-high mass systems ($M_{star} > 10^{11} M_{\odot}$), hence leading to an *upsizing* trend with time in the high-mass end. In our modelling, dry mergers are the main reason for this late assembly of massive galaxies. These findings agree with other previously published semi-analytical models (De Lucia et al., 2006; Cattaneo et al., 2008, 2010). The importance of dry mergers in the formation of the most massive galaxies that we observe in the nearby universe, is implied also by the recent observations of the size evolution of massive spheroids (Trujillo et al., 2007; Cimatti et al., 2008). Indeed, if such compact galaxies are absent in the local universe as suggested by Trujillo et al. (2009), the expected mechanisms that move the high-redshift compact galaxies to the local relation are dissipationless mergers. Anyway, other works (Valentinuzzi et al., 2010) suggest that such superdense galaxies in the local universe are not as rare as previously claimed.

How far this might be incongruous with the observational indication of downsizing in mass assembly mentioned above will become clear with further observational confrontation. For example, Cattaneo et al. (2008) argue that the upsizing

in mass assembly can coexist with a downwards trend in the transition mass, which then turns out to be a poor indicator of downsizing.

In conclusion, GECO presents an encouraging level of agreement with a wide range of observational data, at low and high-redshifts. We focus on comparing GECO with data on the two main phases of the galaxy formation process, that are the star formation and the mass assembly. On one hand, we confirmed that the observed *downsizing* in star formation is natural part of our scheme of hierarchical growth of structures. On the other hand, the stellar mass assembly process remains more difficult to understand from both a theoretical and an observational point of view. The times of galaxy assembly in our model, related with both the galaxy merger time-scales and the star formation efficiency, strongly depend on the details of the implementations of galaxy dynamics (dynamical friction, satellite collisions and tidal stripping): further work in this sense remains to be done in order to have a deeper insight into the galaxy assembly process, and certainly a comparison with N-body simulations will be helpful.

The most striking conclusion is that, despite the simplicity of the prescriptions adopted, and the small number of free parameters used, the main features of the evolving galaxy population are reproduced. In particular, the AGN feedback is needed only to improve the match of the local stellar mass function, but its effect on stellar ages is not determinant.

We have to keep in mind in any case that this paper includes just a preliminary and partial confrontation with the data, showing at least no obvious clash. Much more extensive analyses and tighter constraints will be obtained as soon as refined data on the evolutionary mass functions and stellar birthrates will become available.

Acknowledgements

We thank the referee for helpful suggestion which improved the paper. We are grateful to Nicola Menci for various illuminating discussions, criticisms and suggestions about the present model. We also thank Alfonso Cavaliere and Pierluigi Monaco for discussions and Antonio Cava, Carlo Giocoli and Ignacio Trujillo for helpful suggestions. We acknowledge financial support by the Padova University for the PhD studentship and the Italian Space Agency for funding a post-doc fellowship, which made this paper possible.

References

- Baldry I. K., Glazebrook K., Brinkmann J., Ivezić Ž., Lupton R. H., Nichol R. C., Szalay A. S., 2004, *ApJ*, 600, 681
 Baugh C. M., Cole S., Frenk C. S., 1996, *MNRAS*, 283, 1361
 Bell E. F., McIntosh D. H., Katz N., Weinberg M. D., 2003, *ApJS*, 149, 289
 Bell E. F., Phleps S., Somerville R. S., Wolf C., Borch A., Meisenheimer K., 2006, *ApJ*, 652, 270
 Benson A. J., Lacey C. G., Baugh C. M., Cole S., Frenk C. S., 2002, *MNRAS*, 333, 156
 Benson A. J., Frenk C. S., Baugh C. M., Cole S., Lacey C. G., 2003, *MNRAS*, 343, 679
 Berta S., et al., 2007, *A&A*, 476, 151
 Bertone S., De Lucia G., Thomas P. A., 2007, *MNRAS*, 379, 1143
 Blumenthal G. R., Faber S. M., Primack J. R., Rees M. J., 1984, *Nat*, 311, 517
 Bond J. R., Cole S., Efstathiou G., Kaiser N., 1991, *ApJ*, 379, 440
 Bond J. R., Myers S. T., 1996, *ApJS*, 103, 1
 Bower R. G., Benson A. J., Malbon R., Helly J. C., Frenk C. S., Baugh C. M., Cole S., Lacey C. G., 2006, *MNRAS*, 370, 645
 Boylan-Kolchin M., Ma C.-P., Quataert E., 2008, *MNRAS*, 383, 93
 Bundy K., Ellis R. S., Conselice C. J., 2005, *ApJ*, 625, 621

- Bundy K., et al., 2006, *ApJ*, 651, 120
 Bunker A., et al., 2009, arXiv, arXiv:0909.2255
 Cattaneo A., Dekel A., Devriendt J., Guiderdoni B., Blaizot J., 2006, *MNRAS*, 370, 1651
 Cattaneo A., Dekel A., Faber S. M., Guiderdoni B., 2008, *MNRAS*, 385, 858
 Cattaneo A., Mamon G. A., Warnick K., Knebe A., 2010, arXiv, arXiv:1002.3257
 Chandrasekhar S., 1943, *ApJ*, 97, 255
 Cimatti A., Daddi E., Renzini A., 2006, *A&A*, 453, L29
 Cimatti A., et al., 2008, *A&A*, 482, 21
 Croton D. J., et al., 2006, *MNRAS*, 365, 11
 Cole S., Lacey C., 1996, *MNRAS*, 281, 716
 Cole S., Aragon-Salamanca A., Frenk C. S., Navarro J. F., Zepf S. E., 1994, *MNRAS*, 271, 781
 Cole S., Benson A., Baugh C., Lacey C., Frenk C., 2000, *ASPC*, 200, 109
 Cole S., et al., 2001, *MNRAS*, 326, 255
 Cowie L. L., Songaila A., Hu E. M., Cohen J. G., 1996, *AJ*, 112, 839
 Cox T. J., Jonsson P., Somerville R. S., Primack J. R., Dekel A., 2008, *MNRAS*, 384, 386
 De Lucia G., Kauffmann G., Springel V., White S. D. M., Lanzoni B., Stoehr F., Tormen G., Yoshida N., 2004, *MNRAS*, 348, 333
 De Lucia G., Springel V., White S. D. M., Croton D., Kauffmann G., 2006, *MNRAS*, 366, 499
 Dekel A., Birnboim Y., 2006, *MNRAS*, 368, 2
 Dekel A., Silk J., 1986, *ApJ*, 303, 39
 Dunkley J., et al., 2009, *ApJS*, 180, 306
 Elbaz D., Cesarsky C. J., Chantal P., Aussel H., Franceschini A., Fadda D., Chary R. R., 2002, *A&A*, 384, 848
 Fan X., et al., 2000, *AJ*, 120, 1167
 Ferrarese L., Merritt D., 2000, *ApJ*, 539, L9
 Fontana A., et al., 2006, *A&A*, 459, 745
 Fontanot F., De Lucia G., Monaco P., Somerville R. S., Santini P., 2009, *MNRAS*, 397, 1776
 Franceschini A., Silva L., Fasano G., Granato G. L., Bressan A., Arnouts S., Danese L., 1998, *ApJ*, 506, 600
 Franceschini A., Aussel H., Cesarsky C. J., Elbaz D., Fadda D., 2001, *A&A*, 378, 1
 Franceschini A., et al., 2006, *A&A*, 453, 397
 Gavazzi G., Scodreggio M., 1996, *A&A*, 312, L29
 Gebhardt K., et al., 2000, *ApJ*, 539, L13
 Giocoli C., Moreno J., Sheth R. K., Tormen G., 2007, *MNRAS*, 376, 977
 Gnedin N. Y., 2000, *ApJ*, 542, 535
 Heckman T. M., 2001, *ASPC*, 240, 345
 Häring N., Rix H.-W., 2004, *ApJ*, 604, L89
 Hatton S., Devriendt J. E. G., Ninin S., Bouchet F. R., Guiderdoni B., Vibert D., 2003, *MNRAS*, 343, 75
 Hoeft M., Yepes G., Gottlöber S., Springel V., 2006, *MNRAS*, 371, 401
 Hopkins A. M., 2004, *ApJ*, 615, 209
 Hopkins P. F., Richards G. T., Hernquist L., 2007, *ApJ*, 654, 731
 Hopkins P. F., Bundy K., Hernquist L., Ellis R. S., 2007, *ApJ*, 659, 976
 Jiang C. Y., Jing Y. P., Faltenbacher A., Lin W. P., Li C., 2008, *ApJ*, 675, 1095
 Kang X., van den Bosch F. C., 2008, *ApJ*, 676, L101
 Kauffmann G., Haehnelt M., 2000, *MNRAS*, 311, 576
 Kauffmann G., White S. D. M., 1993, *MNRAS*, 261, 921
 Kauffmann G., White S. D. M., Guiderdoni B., 1993, *MNRAS*, 264, 201
 Kauffmann G., Colberg J. M., Diaferio A., White S. D. M., 1999, *MNRAS*, 307, 529
 Kauffmann G., et al., 2003, *MNRAS*, 341, 54
 Kennicutt R. C., Jr., 1998, *ApJ*, 498, 541
 Kereš D., Katz N., Weinberg D. H., Davé R., 2005, *MNRAS*, 363, 2
 Kimm T., et al., 2009, *MNRAS*, 394, 1131
 Kitzbichler M. G., White S. D. M., 2006, *MNRAS*, 366, 858
 Kravtsov A. V., Gnedin O. Y., Klypin A. A., 2004, *ApJ*, 609, 482
 Lacey C., Cole S., 1993, *MNRAS*, 262, 627
 Lagos C. D. P., Cora S. A., Padilla N. D., 2008, *MNRAS*, 388, 587
 Lanzoni B., Guiderdoni B., Mamon G. A., Devriendt J., Hatton S., 2005, *MNRAS*, 361, 369
 Lapi A., Shankar F., Mao J., Granato G. L., Silva L., De Zotti G., Danese L., 2006, *ApJ*, 650, 42
 Macciò A. V., Kang X., Fontanot F., Somerville R. S., Kaposov S., Monaco P., 2009, *MNRAS*, 397, 1907
 Malbon R. K., Baugh C. M., Frenk C. S., Lacey C. G., 2007, *MNRAS*, 382, 1394
 Mamon G. A., 1992, *ApJ*, 401, L3
 Marchesini D., van Dokkum P. G., Förster Schreiber N. M., Franx M., Labbé I., Wuyts S., 2009, *ApJ*, 701, 1765
 Martin C. L., 1999, *ApJ*, 513, 156
 Marulli F., Bonoli S., Branchini E., Moscardini L., Springel V., 2008, *MNRAS*, 385, 1846
 McCarthy I. G., Frenk C. S., Font A. S., Lacey C. G., Bower R. G., Mitchell N. L., Balogh M. L., Theuns T., 2008, *MNRAS*, 383, 593
 Menci N., Cavaliere A., 2002, *ASPC*, 253, 429
 Menci N., Cavaliere A., Fontana A., Giallongo E., Poli F., Vittorini V., 2004, *ApJ*, 604, 12
 Menci N., Fontana A., Giallongo E., Grazian A., Salimbeni S., 2006, *ApJ*, 647, 753
 Mihos J. C., Hernquist L., 1994, *ApJ*, 425, L13
 Mihos J. C., Hernquist L., 1996, *ApJ*, 464, 641
 Mo H. J., Mao S., White S. D. M., 1998, *MNRAS*, 295, 319
 Monaco P., Fontanot F., Taffoni G., 2007, *MNRAS*, 375, 1189
 Monaco P., et al., 2009, *AIPC*, 1111, 48
 Navarro J. F., White S. D. M., 1994, *MNRAS*, 267, 401
 Navarro J. F., Frenk C. S., White S. D. M., 1995, *MNRAS*, 275, 56
 Navarro J. F., Frenk C. S., White S. D. M., 1997, *ApJ*, 490, 493
 Neistein E., van den Bosch F. C., Dekel A., 2006, *MNRAS*, 372, 933
 Okamoto T., Gao L., Theuns T., 2008, *MNRAS*, 390, 920
 Percival W. J., et al., 2002, *MNRAS*, 337, 1068
 Pérez-González P. G., et al., 2008, *ApJ*, 675, 234
 Perlmutter S., Turner M. S., White M., 1999, *PhRvL*, 83, 670
 Press W. H., Schechter P., 1974, *ApJ*, 187, 425
 Riess A. G., et al., 1998, *AJ*, 116, 1009
 Rodighiero G., et al., 2009, arXiv, arXiv:0910.5649
 Roos N., Norman C. A., 1979, *A&A*, 76, 75
 Sanders D. B., Mirabel I. F., 1996, *ARA&A*, 34, 749
 Shankar F., Salucci P., Granato G. L., De Zotti G., Danese L., 2004, *MNRAS*, 354, 1020
 Sheth R. K., Lemson G., 1999, *MNRAS*, 305, 946
 Sheth R. K., Tormen G., 2002, *MNRAS*, 329, 61
 Sijacki D., Springel V., di Matteo T., Hernquist L., 2007, *MNRAS*, 380, 877
 Somerville R. S., 2002, *ApJ*, 572, L23
 Somerville R. S., Kolatt T. S., 1999, *MNRAS*, 305, 1
 Somerville R. S., Primack J. R., 1999, *MNRAS*, 310, 1087
 Somerville R. S., Primack J. R., Faber S. M., 2001, *MNRAS*, 320, 504
 Somerville R. S., Hopkins P. F., Cox T. J., Robertson B. E., Hernquist L., 2008, *MNRAS*, 391, 481
 Spergel D. N., et al., 2003, *ApJS*, 148, 175
 Spergel D. N., et al., 2007, *ApJS*, 170, 377
 Springel V., Yoshida N., White S. D. M., 2001, *NewA*, 6, 79
 Strickland D. K., Heckman T. M., Weaver K. A., Dahlem M., 2000, *AJ*, 120, 2965
 Stringer M. J., Benson A. J., Bundy K., Ellis R. S., Quetin E. L., 2009, *MNRAS*, 393, 1127
 Sutherland R. S., Dopita M. A., 1993, *ApJS*, 88, 253
 Taffoni G., Mayer L., Colpi M., Governato F., 2003, *MNRAS*, 341, 434
 Tegmark M., et al., 2004, *ApJ*, 606, 702
 Thomas D., Maraston C., Bender R., Mendes de Oliveira C., 2005, *ApJ*, 621, 673
 Thoul A. A., Weinberg D. H., 1996, *ApJ*, 465, 608
 Tormen G., 1997, *MNRAS*, 290, 411
 Trujillo I., Cenarro A. J., de Lorenzo-Cáceres A., Vazdekis A., de la Rosa I. G., Cava A., 2009, *ApJ*, 692, L118
 Trujillo I., Conselice C. J., Bundy K., Cooper M. C., Eisenhardt P., Ellis R. S., 2007, *MNRAS*, 382, 109
 Valentinuzzi T., et al., 2010, *ApJ*, 712, 226
 van Dokkum P. G., 2005, *AJ*, 130, 2647
 Viola M., Monaco P., Borgani S., Murante G., Tornatore L., 2008, *MNRAS*, 383, 777
 Volonteri M., Lodato G., Natarajan P., 2008, *MNRAS*, 383, 1079
 Warren M. S., Quinn P. J., Salmon F. K., Zurek W. H., 1992, *ApJ*, 399, 405
 Weinmann S. M., van den Bosch F. C., Yang X., Mo H. J., Croton D. J., Moore B., 2006, *MNRAS*, 372, 1161
 White S. D. M., Frenk C. S., 1991, *ApJ*, 379, 52
 White S. D. M., Rees M. J., 1978, *MNRAS*, 183, 341
 White S. D. M., Navarro J. F., Evrard A. E., Frenk C. S., 1993, *Nat*, 366, 429
 Zentner A. R., 2007, *IJMPD*, 16, 763
 Zhang J., Ma C.-P., Fakhouri O., 2008, *MNRAS*, 387, L13

Appendix A: Effect of AGN feedback

Several recent works (Croton et al., 2006; Malbon et al., 2007; Sijacki et al., 2007) advocated the AGN feedback as the only mechanism able to quench star formation in order to match the local abundance of massive galaxies as well as their old ages and red colours. Here we check the relevance of such feedback in reproducing the observations in GECO, comparing our fiducial model with a version in which the AGN feedback (both in quasar and radio modes) is switched off. In Figure A.1 we can see the effect of the AGN in the stellar mass function. As expected, the presence of the AGN influences only the bright-end, reducing it by ≈ 0.15 dex, both in the local universe (upper panel) and at high redshift (lower panel), hence leading to the same amount of evolution in the stellar mass function as in the fiducial case. We note that given the overabundance of massive galaxies by the same amount at all the redshift, in the model without AGN the comparison with the observational mass function at high redshift results in a closer agreement with respect to the fiducial model. Figure A.2 shows that, obviously, in the model without AGN the star formation keeps lower at all redshifts, with an indication that at very high redshift ($z > 4$) the difference between the two models tends to disappear, meaning that the importance of AGN feedback increases at late cosmic times.

A further issue to be handled is the relevance of the AGN in producing the downsizing trend in the stellar ages. In Figure A.3 the trend of the formation redshift with mass is shown for both models. Although the AGN is effective in increasing stellar ages, the net effect is actually very modest. At variance with other models (Croton et al. 2006 for instance) the downsizing trend is still recovered, leading to the conclusion that the presence of AGN is not the main reason for the onset of the downsizing pattern for galaxy evolution in our model.

Therefore, in our model the AGN has the effect of reducing the star formation activity in the high-mass objects, but the amount of reduction is perhaps less striking than previously claimed (Croton et al., 2006; Malbon et al., 2007; Marulli et al., 2008; Lagos, Cora, & Padilla, 2008). Indeed, the values for the efficiencies of black hole accretion adopted here, are somehow smaller than those adopted by the models mentioned above, but we found that they are suitable to obtain the very good match of the local relations.

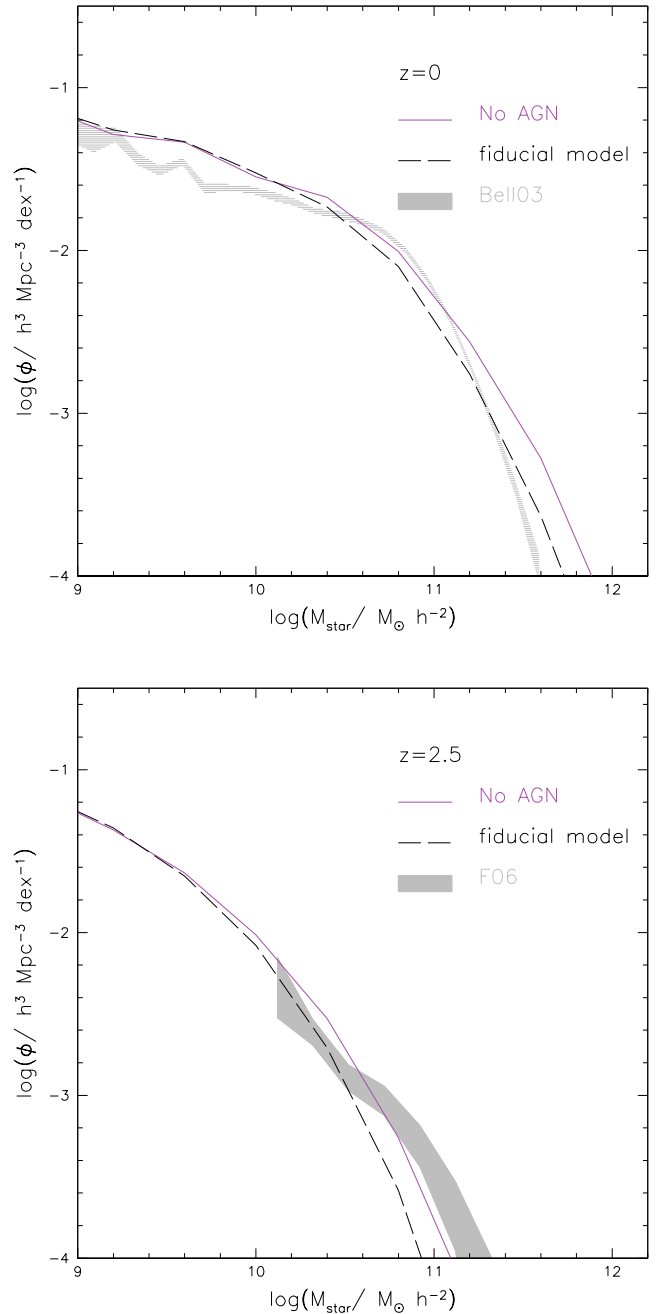


Fig. A.1. Upper panel: comparison between the stellar mass function at $z=0$ of our fiducial model (dashed black line) with the model without AGN feedback (solid purple line). Lower panel: the same as the upper panel but for $z=2.5$. Observational data at the given redshift are also indicated by the shaded region.

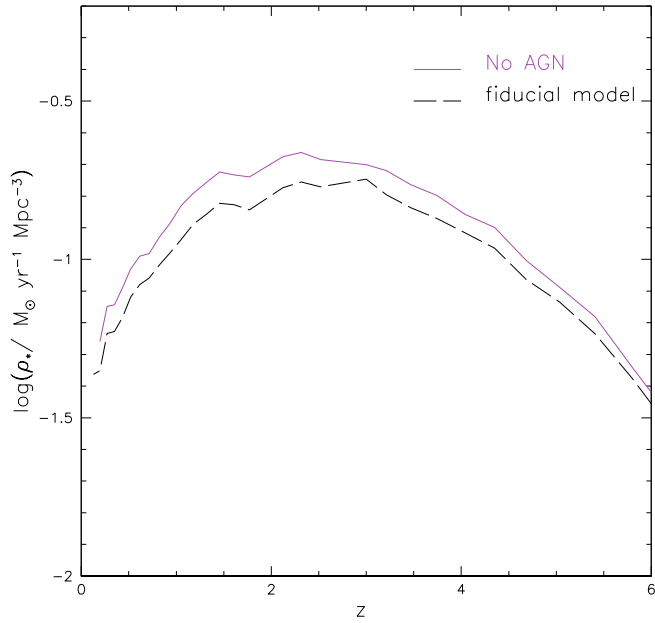


Fig. A.2. Comparison between the SFR density as a function of redshift in the model without AGN feedback (solid purple line) and the fiducial case (dashed black line).

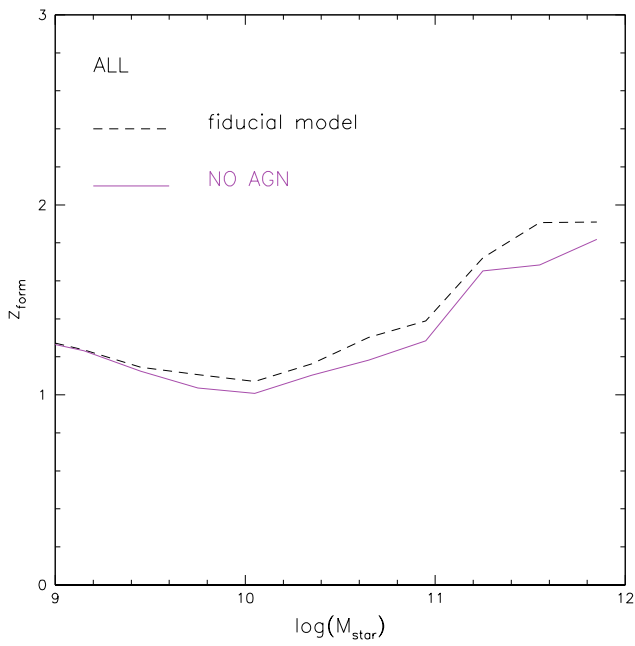


Fig. A.3. Comparison between the formation redshifts as a function of stellar mass in the model without AGN feedback (solid purple line) and the fiducial case (dashed black line).

Appendix B: Effect of cosmic reionization

As explained in Sect. 3.5.2, our treatment for the cosmic reionization is based on the results previously found by Benson et al. (2003). Anyway, it has been claimed, on the basis of recent hydrodynamical simulations, that the effect of the photoionizing background on structure formation is indeed weaker than previously assumed (Hoeft et al., 2006; Okamoto, Gao, & Theuns, 2008). Taking into account such results, we test the effect of our assumption on the limit circular velocity for the reionization. In Figure B.1 we show a comparison between our fiducial model with a model in which the circular velocity limit for baryon cooling has been lowered down to 25 km/s. To allow the formation of low-mass halos, we used for this model a merger tree with a resolution of $10^9 M_\odot$. We see that a lower limit on the circular velocity has the effect of slightly increasing the number of low mass galaxies. At the same time, the number of massive objects is reduced, since a greater amount of gas has been locked within satellites and is not available for star formation inside the brightest systems. In any case, the effect is rather moderate and the prediction of the fiducial model could be accommodated, for instance, by increasing the effect of SN.

Therefore, we conclude that although we might have over-estimated the effect of reionization in our fiducial model, the main results found in the previous sections keep unchanged if we allow a milder dependence of galaxy formation on the cosmic reionization.

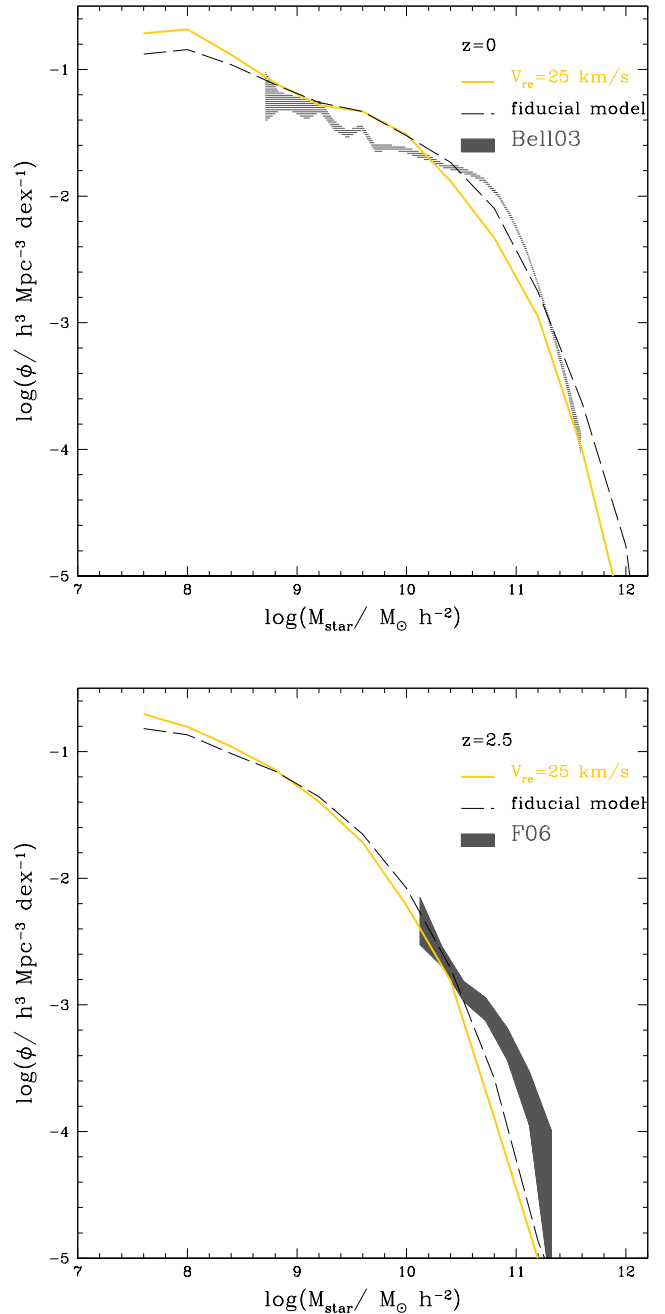


Fig. B.1. Upper panel: comparison between the stellar mass function at $z=0$ of our fiducial model (dashed black line) with a model with a reduced effect of the cosmic reionization (solid yellow line). Lower panel: the same as the upper panel but for $z=2.5$. Observational data at the given are also indicated by the shaded region.